Monthly Notices
of the
ROYAL ASTRONOMICAL SOCIETY

MNRAS **506,** 5935–5950 (2021)
Advance Access publication 2021 July 19

https://doi.org/10.1093/mnras/stab2052

A hard X-ray view of luminous and ultra-luminous infrared galaxies in GOALS – I. AGN obscuration along the merger sequence

C. Ricci [1,2★] G. C. Privon [3] R. W. Pfeifle,[4] L. Armus,[5] K. Iwasawa,[6,7] N. Torres-Albà,[8] S. Satyapal,[4] F. E. Bauer,[9,10,11] E. Treister,[9] L. C. Ho,[2,12] S. Aalto,[13] P. Arévalo,[14] L. Barcos-Muñoz,[3] V. Charmandaris,[15,16] T. Diaz-Santos,[15,16] A. S. Evans,[17,3] T. Gao,[18] H. Inami,[19] M. J. Koss [20] G. Lansbury [21] S. T. Linden,[22] A. Medling [23,24] D. B. Sanders,[25] Y. Song,[17] D. Stern,[26] V. U,[27] Y. Ueda[28] and S. Yamada[28]

Affiliations are listed at the end of the paper

Accepted 2021 July 9. Received 2021 July 2; in original form 2021 May 20

ABSTRACT

The merger of two or more galaxies can enhance the inflow of material from galactic scales into the close environments of active galactic nuclei (AGNs), obscuring and feeding the supermassive black hole (SMBH). Both recent simulations and observations of AGN in mergers have confirmed that mergers are related to strong nuclear obscuration. However, it is still unclear how AGN obscuration evolves in the last phases of the merger process. We study a sample of 60 luminous and ultra-luminous IR galaxies (U/LIRGs) from the GOALS sample observed by *NuSTAR*. We find that the fraction of AGNs that are Compton thick (CT; $N_{\rm H} \geq 10^{24}\,{\rm cm}^{-2}$) peaks at 74^{+14}_{-19} per cent at a late merger stage, prior to coalescence, when the nuclei have projected separations ($d_{\rm sep}$) of 0.4–6 kpc. A similar peak is also observed in the median $N_{\rm H}$ [$(1.6 \pm 0.5) \times 10^{24}\,{\rm cm}^{-2}$]. The vast majority ($85^{+7}_{-9}$ per cent) of the AGNs in the final merger stages ($d_{\rm sep} \lesssim 10$ kpc) are heavily obscured ($N_{\rm H} \geq 10^{23}\,{\rm cm}^{-2}$), and the median $N_{\rm H}$ of the accreting SMBHs in our sample is systematically higher than that of local hard X-ray-selected AGN, regardless of the merger stage. This implies that these objects have very obscured nuclear environments, with the $N_{\rm H} \geq 10^{23}\,{\rm cm}^{-2}$ gas almost completely covering the AGN in late mergers. CT AGNs tend to have systematically higher absorption-corrected X-ray luminosities than less obscured sources. This could either be due to an evolutionary effect, with more obscured sources accreting more rapidly because they have more gas available in their surroundings, or to a selection bias. The latter scenario would imply that we are still missing a large fraction of heavily obscured, lower luminosity ($L_{2-10} \lesssim 10^{43}\,{\rm erg\,s}^{-1}$) AGNs in U/LIRGs.

Key words: galaxies: active – quasars: general – galaxies: Seyfert – infrared: galaxies – X-rays: general.

1 INTRODUCTION

The discovery of a correlation between the mass of supermassive black holes (SMBHs) and several properties of their host galaxies (e.g. Magorrian et al. 1998; Ferrarese & Merritt 2000; Gebhardt et al. 2000; Kormendy & Ho 2013) has suggested that the growth of SMBHs and their host galaxies are tightly connected. Mergers of galaxies are thought to be one of the most important mechanisms with which galaxies build up their stellar masses (White & Rees 1978). Both observational (e.g. Lonsdale, Persson & Matthews 1984; Joseph & Wright 1985; Armus, Heckman & Miley 1987; Clements et al. 1996; Alonso-Herrero et al. 2000; Ellison et al. 2008) and theoretical (e.g. Mihos & Hernquist 1996; Di Matteo et al. 2007) studies have shown that galaxy mergers enhance star formation (SF). Simulations have also shown that the interaction between two or more galaxies can reduce the angular momentum of the circumnuclear material (e.g. Barnes & Hernquist 1991; Blumenthal & Barnes 2018), thus providing an effective mechanism to trigger accretion on to SMBHs (e.g. Di Matteo, Springel & Hernquist 2005). Observationally, several works have confirmed this scenario. Koss et al. (2010) and Silverman et al. (2011) found a higher AGN fraction in pairs than in isolated galaxies with similar stellar masses. It has been shown that the fraction of AGN in mergers tends to increase as the separation between the two galaxies decreases (Ellison et al. 2011), and peaks after coalescence (Ellison et al. 2013). Koss et al. (2012) have shown that the average luminosity of dual AGN also increases with decreasing separation (see also Hou, Li & Liu 2020), and it is higher for the primary (i.e. more massive) component of the system (see also De Rosa et al. 2019, for a recent review). While AGNs with moderate X-ray luminosities are typically found in non-interacting disc galaxies (e.g. Koss et al. 2011; Kocevski et al. 2012; Schawinski et al. 2012), more luminous objects are commonly found in merging systems (e.g. Treister et al. 2012; Glikman et al. 2015; Hong et al. 2015). Treister et al. (2012) showed that, while for 2–10 keV AGN luminosities of $L_{2-10} \sim 10^{41}\,{\rm erg\,s}^{-1}$ only a small fraction (<1 per cent) of AGNs are in mergers, at $L_{2-10} \sim 10^{46}\,{\rm erg\,s}^{-1}$ ∼ 70–80 per cent of the sources are found in interacting systems (see also Glikman et al. 2015). Recent evidence has suggested that hot dust obscured galaxies (Hot DOGs; Wu et al.

★ E-mail: claudio.ricci@mail.udp.cl

2012; Assef et al. 2015), which are some of the most luminous galaxies observed so far ($L_{\rm IR} > 10^{13} L_{\odot}$), are also found in mergers (e.g. Fan et al. 2016). These observations suggest that, while at low luminosities SMBH accretion is triggered by secular processes, at high luminosities mergers can play a dominant role. This is in agreement with the evolutionary scenario proposed by Sanders et al. (1988) for ultra-luminous [$L_{\rm IR}(8–1000\,\mu{\rm m}) \geq 10^{12}\,L_{\odot}$] infrared galaxies (ULIRGs; e.g. Sanders & Mirabel 1996; Pérez-Torres et al. 2021). In this scheme, two gas-rich disc galaxies collide, triggering SF and accretion on to the SMBH. The strong accretion on to the SMBH would lead the source to evolve first in a luminous red quasar (e.g. Urrutia, Lacy & Becker 2008; Glikman et al. 2015; LaMassa et al. 2016) and then in an unobscured blue quasar.

The bulk of the growth of SMBHs during mergers is believed to be very obscured. This has been shown by numerical simulations (e.g. Hopkins et al. 2008; Blecha et al. 2018; Kawaguchi, Yutani & Wada 2020), as well as by recent observations. Satyapal et al. (2014) have shown that post-mergers host a significantly higher fraction of mid-IR-selected AGNs than optical AGNs, which could suggest that optically obscured AGNs become prevalent in the most advanced mergers (see also Koss et al. 2010; Ellison et al. 2019; Secrest et al. 2020). Kocevski et al. (2015) have shown that heavily obscured ($N_{\rm H} \geq 10^{23.5}\,{\rm cm}^{-2}$) systems are more common in mergers than in isolated galaxies. In the local Universe, major galaxy mergers give rise to luminous infrared galaxies [LIRGS; $L_{\rm IR}(8–1000\,\mu{\rm m}) = 10^{11}–10^{12}\,L_{\odot}$] and ULIRGs that, over the past two decades, have been extensively studied in the IR, optical, and soft (0.3–10 keV) X-ray bands (e.g. Veilleux et al. 1995; Veilleux, Kim & Sanders 1999; Imanishi & Dudley 2000; Imanishi 2002; Franceschini et al. 2003; Alonso-Herrero et al. 2006, 2012; Imanishi, Dudley & Maloney 2006; Armus et al. 2007, 2009; Teng and Veilleux 2010;Nardini & Risaliti 2011; Pereira-Santaella et al. 2011; Armus, Charmandaris & Soifer 2020). Mid-IR observations have suggested the presence of a heavily buried AGN in U/LIRGs, particularly in those undergoing the final stages of mergers (e.g. Imanishi et al. 2007; Veilleux et al. 2009; Nardini et al. 2010). Hard X-ray ($\geq$10 keV) observations can be extremely effective in detecting heavily obscured AGNs and, combined with soft X-ray observations ($<$10 keV), in estimating their line-of-sight column density (e.g. Burlon et al. 2011; Annuar et al. 2015; Ricci et al. 2015, 2017c; Koss et al. 2016a, b). U/LIRGs were studied in the hard X-ray band using *Swift*/BAT by Koss et al. (2013), who suggested that a large fraction of sources might have Compton-thick (CT) column densities. Exploiting the revolutionary capabilities of *NuSTAR*, the first focusing hard X-ray satellite on orbit, Ricci et al. (2017b) studied 30 nearby U/LIRGs from the Great Observatories All-sky LIRG Survey (GOALS; Armus et al. 2009) sample.[1] Ricci et al. (2017b) showed that 65^{+12}_{-13} per cent of the AGNs in objects in late-stage mergers (i.e. with projected separations of $d_{\rm sep} \simeq 10$ kpc) are CT ($N_{\rm H} \geq 10^{24}$ cm), a fraction significantly higher than what is found for local hard X-ray-selected AGNs (27 ± 4 per cent; Ricci et al. 2015), which are typically found in non-interacting systems. Similar results have also been found by several other studies, which find that AGNs in mergers are systematically more obscured than those in isolated galaxies (e.g. Nardini & Risaliti 2011; Lanzuisi et al. 2015; Del Moro et al. 2016; Koss et al. 2016a, 2018; Satyapal et al. 2017; Dutta et al. 2018, 2019;Donley et al. 2018; Goulding et al. 2018; Pfeifle et al. 2019a, b; Secrest et al. 2020; Foord et al. 2021; Guainazzi et al. 2021). At higher luminosities and redshifts, X-ray observations of Hot DOGs have shown that these powerful AGNs are also typically very obscured (e.g. Piconcelli et al. 2015; Ricci et al. 2017a; Zappacosta et al. 2018; Toba et al. 2020).

.

While a growing number of observations have demonstrated that the obscuration properties of AGN in mergers are very different from those of AGN in isolated galaxies (see Ramos Almeida & Ricci 2017; Hickox & Alexander 2018, for recent reviews), it is still unclear how AGN obscuration evolves in the last phases of the merger process, when the two nuclei are at a projected separation of $d_{\rm sep} < 10$ kpc. With the goal of addressing this important issue, and to increase the number of sources with $d_{\rm sep} < 10$ kpc, in this work we double, with respect to Ricci et al. (2017b), the number of U/LIRGs from the GOALS sample observed in the hard X-rays by *NuSTAR*. GOALS is a sample of nearby ($z < 0.088$) galaxies detected by the *Infrared Astronomical Satellite* (*IRAS*) revised bright Galaxy Survey (Sanders et al. 2003), which has a very wealthy collection of ancillary data across the whole multiwavelength spectrum (e.g. Howell et al. 2010; Petric et al. 2011; Stierwalt et al. 2013). Exploiting the excellent constraints on the AGN obscuration obtained by broad-band X-ray observations, we study here the relation between obscuration and merger stage, focusing in particular on the final stages of the merger process. A companion paper (Yamada et al. 2021) focuses on the physical X-ray modelling of these sources, to constrain the covering factor of the torus from X-ray spectroscopy, and on the X-ray-to-bolometric AGN luminosity ratios, to further discuss their nuclear properties in comparison with normal AGNs.

The paper is structured as follows: In Section 2, we describe our sample. In Section 3, we present the X-ray data used and the methodology for the data reduction. In Section 4, we discuss the spectral analysis of the sources. In Section 5, we discuss the relation between mergers and AGN obscuration. Our main results are summarized in Section 6. Throughout the paper, we adopt standard cosmological parameters ($H_0 = 70\,{\rm km\,s^{-1}\,Mpc^{-1}}$, $\Omega_{\rm m} = 0.3$, and $\Omega_{\Lambda} = 0.7$). Unless otherwise stated, uncertainties are quoted at the 90 per cent confidence level.

2 SAMPLE

The all-sky GOALS sample consists of 180 LIRGs and 22 ULIRGs, and is complete at 60 μm for fluxes $>$5.24 Jy. Objects in GOALS have been extensively studied in the IR, with a large number of observations carried out by *Spitzer*, *Akari*, and *Herschel* (e.g. Inami et al. 2010, 2013, 2018; Díaz-Santos et al. 2011; Petric et al. 2011; U et al. 2012, 2019; Stierwalt et al. 2013, 2014; Medling et al. 2014; Lu et al. 2017). Moreover, a large *Chandra* campaign provides spectroscopic coverage in the 0.3–10 keV range, as well as high-spatial resolution images in the same band (Iwasawa et al. 2011; Torres-Albà et al. 2018). Our sample includes all U/LIRGs from the GOALS sample that were observed by *NuSTAR*. This includes the 30 objects reported in Ricci et al. (2017b), besides sources that were recently analysed in literature studies, as well as 19 objects that have been recently observed by *NuSTAR* as a part of several observational campaigns led by our team (PIs: Ricci, C; Privon, G.; Armus, L.) to study SMBH accretion in the final phases of the merger process. Overall, our sample contains 60 U/LIRGs.

2.1 Merger stages

Near-infrared (NIR) and mid-infrared (MIR) images were used to classify the sources into different merger stages. We followed what was reported by Haan et al. (2011) using *HST* images and, when

[1] http://goals.ipac.caltech.edu/

that was not available, we considered the classification of Stierwalt et al. (2013), including the modifications proposed by Ricci et al. (2017b). Based on the morphological properties of the objects, we divided them into five different merger stages, following Stierwalt et al. (2013):

Stage *a*: galaxy pairs before a first encounter.
Stage *b*: galaxies after a first encounter, with symmetric galaxy discs but showing signs of tidal tails.
Stage *c*: systems showing strong tidal tails, amorphous discs, and other signs of merger activity.
Stage *d*: galaxies in the final merger stages, with the two nuclei being in a common envelope or showing only a single nucleus.
Stage *N*: sources that do not appear to be in a major merger. These sources could either be post-mergers or minor mergers.

Sources in the early merger stages are classified as belonging to the *a* and *b* class, while those in late-stage mergers have been classified as being in the *c* or *d* stage (see Stierwalt et al. 2013, for details, and fig. 1 of Ricci et al. 2017b). Typically, sources in late-stage mergers are separated by $d_{\rm sep} \lesssim 11$ kpc. All the sources in our sample, together with their merger stages and the projected distances between the two nuclei, are listed in Table 1, while in Fig. 1 we illustrate some of their main properties. The closest observed projected distance for systems showing at least an AGN is $d_{\rm sep} = 0.4$ kpc; therefore, we assign this distance as the minimum distance between two potential AGNs in this study. Of the 60 sources in our sample, 7 are in stage *a*, 8 in stage *b*, 13 in stage *c*, 21 in stage *d*, and 11 in stage *N*. This doubles the number of U/LIRGS with *NuSTAR* observations with respect to the sample presented in Ricci et al. (2017b), and in particular we have now observations of 34 late-stage galaxies, while only 17 were reported in Ricci et al. (2017b).

2.2 Star formation rates

The star formation rates (SFRs) and IR luminosities were taken from Díaz-Santos et al. (2017). The SFRs were obtained based on the host galaxy IR luminosity (excluding the AGN contribution estimated by Díaz-Santos et al. 2017), using the relation reported by Murphy et al. (2011). We privileged these values rather than the more recent compilation of Shangguan et al. (2019), since it allowed us to recover the SFRs for the individual galactic nuclei. We tested the SFRs of Shangguan et al. (2019), and found results consistent with those we obtained using the aforementioned approach. For three objects in our sample, which were not reported in Díaz-Santos et al. (2017), we used values from recent literature. For NGC 1068 and NGC 1365, we used the SFRs obtained by Ichikawa et al. (2017, 2019), while for the Hickson compact Group 16 (Hickson 1982) we used the values reported in O'Sullivan et al. (2014) and Bitsakis et al. (2014).

2.3 Comparison sample

As a comparison sample, similarly to what was done in Ricci et al. (2017b), we use AGNs reported in the *Swift*/BAT 70-month catalogue (Baumgartner et al. 2013), which were selected in the 14–195 keV band. Studying optical images, Koss et al. (2010) showed that only ∼25 per cent of the AGNs detected by BAT are found in major mergers with a nuclear separation $d_{\rm sep} \lesssim 100$ kpc. The broad-band (0.3–150 keV) X-ray spectra of these ∼840 AGNs have been analysed in detail by Ricci et al. (2017c), who reported values of the column density for ∼99.8 per cent of them. The obscuration properties of the ∼730 non-blazar AGNs in the sample were discussed in Ricci et al. (2015, 2017d), who found that 27 ± 4 per cent of the objects are CT, and 70 per cent of them are obscured [$\log(N_{\rm H}/{\rm cm}^{-2}) \geq 22$].

3 DATA REDUCTION

In this work, we analyse X-ray data obtained from the *NuSTAR*, *Chandra*, and *XMM–Newton* facilities, the data reduction of which we outline in Sections 3.1, 3.2, and 3.3, respectively. The extraction regions of the different instruments were selected to cover the host galaxies. We combine these with similar X-ray data previously analysed and presented in Ricci et al. (2017b) for 30 GOALS U/LIRGs, and literature constraints on several additional objects. The details of all X-ray observations analysed here are listed in Table A1.

3.1 *NuSTAR*

We analyse *NuSTAR* (Harrison et al. 2013) observations for 23 sources using the *NuSTAR* Data Analysis Software NUSTARDAS v1.9.2 within HEASOFT v6.27. We adopted the calibration files released on 2020 May 6 (Madsen et al. 2015). In order to extract the source spectra, we use a circle of 50 arcsec, while for the background we consider an annulus centred on the source, with inner and outer radii of 60 and 100 arcsec, respectively. In several cases, no X-ray source is detected by *NuSTAR*, and for these sources we follow the same approach reported in Lansbury et al. (2017) to calculate the flux upper limits. This is done using the Bayesian approach of Kraft, Burrows & Nousek (1991).

3.2 *Chandra*

Chandra/ACIS (Weisskopf et al. 2000; Garmire et al. 2003) observations are available for all of the new sources of our sample. We reduce the observations following standard procedures, using CIAO v.4.10. We reprocess all data sets using the CHANDRA_REPRO task, and then extract the spectra using a circular region with a radius of 10 arcsec. For the background spectra, we used a circular region with the same radius, selected in region devoid of other X-ray sources. In the case of IC 1623B, due to its extended emission, we used a radius of 20 arcsec, for the source, in order to consider all the X-ray emission from the source, consistent with what was done to obtain the *NuSTAR* and *XMM–Newton* spectra; considering a smaller radius (10 arcsec) we obtained similar results for this source (i.e. no clear sign of AGN activity). For IRAS 14348−1447 and IRAS 20550+1655, we also extracted the X-ray emission from the individual nuclei, considering source regions of 1.8 and 2.0 arcsec, respectively. Among the new sources of our sample, only ESO 203−IG001 was not detected by *Chandra*.

3.3 *XMM–Newton*

We include *XMM–Newton* (Jansen et al. 2001) observations for nine sources. The EPIC/PN (Strüder et al. 2001) spectra are obtained by first reducing the original data files using *XMM–Newton* Standard Analysis Software (SAS) version 18.0.0 (Gabriel et al. 2004), and then using the `epchain` task. We filter all observations to remove periods of high-background activity, by analysing the EPIC/PN background light curve in the 10–12 keV band. Finally, the spectra are extracted by using a circular region of 25 arcsec radius, while the background is extracted on the same CCD, in a region devoid of X-ray sources, using a circular region of 40 arcsec radius. None of the observations is significantly affected by pile-up.

Table 1. Sample of 60 U/LIRGs from GOALS with *NuSTAR* observations. (1) *IRAS* name, (2) counterparts, (3) redshift, (4) merger stage, (5) projected separation between the two nuclei in arcsec and (6) in kpc, (7) star formation rate (SFR) estimated from the IR luminosity excluding AGN contribution, and (8) 8–1000 μm IR luminosity. In (5) and (6), we report 'S' for objects for which a single nucleus is observed. The sources classified as *a* and *b* are early-stage mergers, while those in *c* and *d* are late-stage mergers. Sources in the *N* class are those that do not show any clear sign of merger. In the objects in which more than one SFR or IR luminosity are reported, we listed the values for both nuclei.

(1) *IRAS* name	(2) Source	(3) z	(4) M	(5) d_{sep} (arcsec)	(6) d_{sep} (kpc)	(7) SFR ($M_\odot$ yr^{-1})	(8) $\log(L_{IR}/L_\odot)$
F00085−1223	NGC 34	0.0196	*d*	S	S	44.2	11.49
F00163−1039	Arp 256 (MCG−02−01−051 and MCG−02−01−052)	0.0272	*b*	64.3	37.1	37.8/4.2	11.44/10.45
F00344−3349	ESO 350−IG038	0.0206	*c*	3.1	1.1	21.8	11.28
F00506+7248	MCG+12−02−001	0.0157	*c*	0.9	0.3	43.7	11.50
F01053−1746	VV 114 (IC 1623A and IC 1623B)	0.0203	*c*	10.5	4.5	54.6	11.62
F02069−1022	NGC 833 and NGC 835	0.0129	*a*	55.9	15.7	7.8/1.7	10.80/10.02
F02401−0013	NGC 1068	0.0038	*N*	–	–	17.3	11.40
F03117+4151	Mrk 1073	0.0233	*N*	–	–	19.2	11.41
F03164+4119	NGC 1275	0.0176	*N*	–	–	15.1	11.26
F03316−3618	NGC 1365	0.0055	*N*	–	–	17.9	11.00
F04454−4838	ESO 203−IG001	0.0529	*b*	7.4	8.5	68.3	11.86
F05054+1718	CGCG 468−002 (E and W)	0.0182	*b*	29.7	11.3	15.4/4.0	11.03/10.72
F05189−2524	IRAS 05189−2524	0.0426	*d*	S	S	86.1	12.16
F06076−2139	IRAS F06076−2139 (S and N)	0.0375	*c*	7.8	6.2	51.8/7.1	11.59/10.73
07251−0248	–	0.0875	*d*	S	S	315	12.39
F08354+2555	NGC 2623	0.0185	*d*	S	S	52.8	11.59
F08520−6850	ESO 060−IG16 (NE and SW)	0.0463	*c*	9.4	9.4	64.0/11.6	11.75/11.00
F08572+3915	IRAS 08572+3915 (NW and SE)	0.0584	*d*	4.4	5.6	114.9	12.16
F09111−1007	IRAS F09111−1007 (W and E)	0.0541	*b*	36.4	43.4	136/38	11.96/11.40
F09320+6134	UGC 05101	0.0394	*d*	S	S	114.7	12.01
F09333+4841	MCG+08−18−013 and MCG+08−18−012	0.0259	*a*	65.6	36.0	24.7/1.4	11.32/9.98
F10015−0614	NGC 3110 and MCG−01−26−013	0.0169	*a*	108.9	37.7	31.9/3.9	11.38/10.42
F10038−3338	IRAS F10038−3338	0.0341	*d*	S	S	70.3	11.78
F10257−4339	NGC 3256	0.0094	*d*	5.1	1.0	61.1	11.64
F10565+2448	IRAS 10565+2448W	0.0431	*c*	7.4	6.7	172.5	12.08
F11257+5850	Arp 299 (NGC 3690W and NGC 3690E)	0.0102	*c*	22.2	4.7	50.4/53.9	11.67/11.58
F12043−3140	ESO 440−IG058 (N and S)	0.0234	*b*	13.4	6.6	4.6/33.6	10.49/11.38
F12112+0305	–	0.0733	*c*	3.5	5.6	322.5	12.36
F12243−0036	NGC 4418	0.0073	*N*	–	–	11.9	11.19
F12540+5708	Mrk 231	0.0422	*d*	S	S	259.7	12.57
F12590+2934	NGC 4922 (N and S)	0.0232	*c*	22.3	10.9	29.2/0.48	11.37/9.51
13120−5453	IRAS 13120−5453	0.0308	*d*	S	S	299.4	12.32
F13126+2453	IC 860	0.0112	*N*	–	–	19.1	11.14
F13188+0036	NGC 5104	0.0186	*N*	–	–	24.7	11.27
F13197−1627	MCG−03−34−064 and MCG−03−34−063	0.0213	*a*	106.4	37.8	2.7/6.2	11.17/10.61
F13229−2934	NGC 5135	0.0137	*N*	–	–	22.5	11.30
F13362+4831	NGC 5256 (SW and NE)	0.0279	*c*	10.2	6.0	25.8/15.4	11.35/11.13
F13428+5608	Mrk 273	0.0378	*d*	0.9	0.7	166.0	12.21
F14348−1447	F14348−1447 (NE and SW)	0.0830	*c*	4.0	7.3	327.1	12.383
F14378−3651	IRAS 14378−3651	0.0676	*d*	S	S	238.5	12.23
F14544−4255	IC 4518A and IC 4518B	0.0163	*b*	44.7	15.3	21.5/4.0	11.16/10.43
F15250+3608	–	0.0552	*d*	S	S	146.1	12.08
F15327+2340	Arp 220 (W and E)	0.0181	*d*	1.0	0.4	254.1	12.27
F16504+0228	NGC 6240 (N and S)	0.0245	*d*	1.4	0.7	112.1	11.93
F16577+5900	NGC 6286 and NGC 6285	0.0183	*b*	91.1	35.8	26.2/9.8	11.30/10.85
F17138−1017	IRAS F17138−1017	0.0173	*d*	S	S	42.5	11.49
F17207−0014	–	0.0428	*d*	S	S	405.0	12.46
F18293−3413	IRAS F18293-3413	0.0182	*N*	–	–	106.5	11.88
F19297−0406	–	0.0857	*d*	S	S	402.1	12.45
F20221−2458	NGC 6907	0.0106	*N*	–	–	17.6	11.11
20264+2533	MCG +04−48−002 and NGC 6921	0.0139	*a*	91.4	27.1	12.6/7.9	11.01/10.73
F20550+1655	CGCG 448−020 (E and W)	0.0359	*c*	5.0	3.8	83.0/30.6	11.77/11.34
F20551−4250	ESO 286−IG19	0.0430	*d*	S	S	130.9	12.06
F21453−3511	NGC 7130	0.0162	*d*	S	S	30.3	11.42
F23007+0836	Arp 298 (NGC 7469 and IC 5283)	0.0163	*a*	79.7	26.8	43.3/9.2	11.58/10.79

Table 1 – *continued*

(1) *IRAS* name	(2) Source	(3) z	(4) M	(5) d_{sep} (arcsec)	(6) d_{sep} (kpc)	(7) SFR ($M_\odot$ yr^{-1})	(8) log ($L_{IR}/L_\odot$)
F23128−5919	ESO 148−IG002	0.0446	*c*	4.7	4.5	139.5	12.06
F23157+0618	NGC 7591	0.0165	*N*	–	–	17.7	11.11
F23254+0830	Arp 182 (NGC 7674 and NGC 7674A)	0.0289	*b*	34.1	20.7	13.5/2.0	11.54/10.14
23262+0314	NGC 7679 and NGC 7682	0.0171	*a*	269.7	97.3	16.0/–	11.11/–
F23365+3604	–	0.0645	*d*	S	S	224.3	12.20

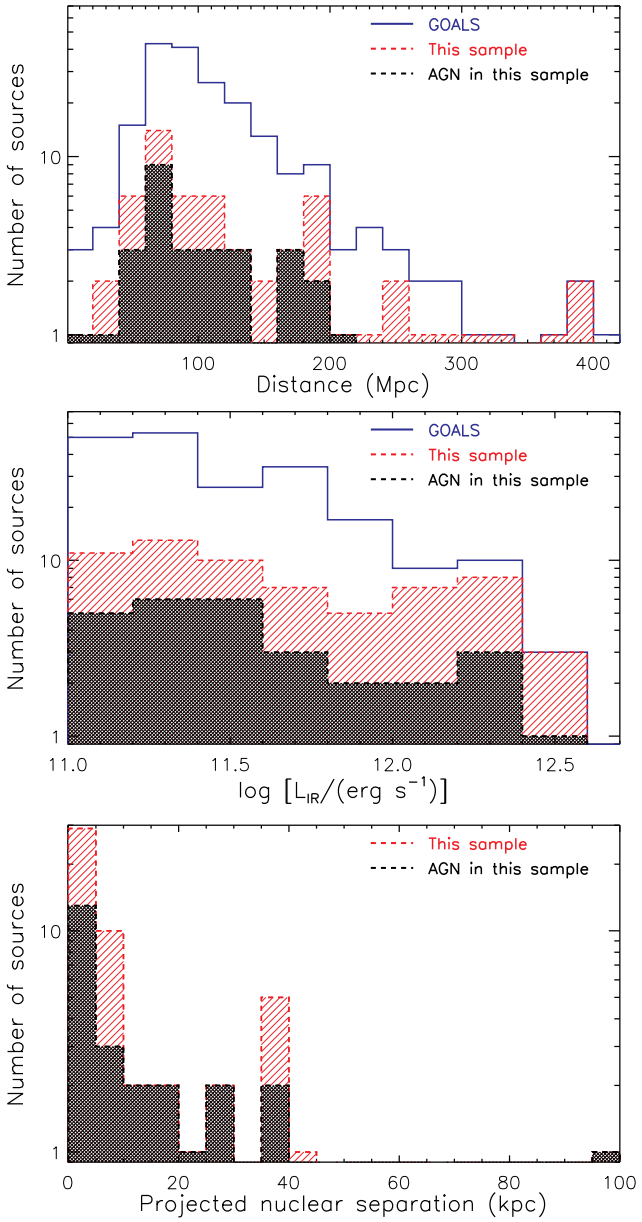

Figure 1. Top panel: Histogram of the distance to the objects in the GOALS sample (blue continuous line), to our sample (red dashed line), and to the X-ray AGN in our sample (black dashed line). Middle panel: Histogram of the 8–1000 μm IR luminosity. Bottom panel: Histogram of the projected separation between the two nuclei of the merging galaxies.

4 X-RAY SPECTRAL ANALYSIS

4.1 Spectral modelling

We fit the X-ray spectra of all sources starting with an SF model, which consists of a power-law component (ZPOW in XSPEC) and a collisionally ionized plasma (APEC). We include Galactic absorption using the TBABS model (Wilms, Allen & McCray 2000), fixing the column density to the value reported by Kalberla et al. (2005) at the coordinates of the source. Intrinsic absorption is considered by including a ZTBABS component. Overall, the SF model used is: TBABS×ZTBABS×(ZPOW+APEC). In a few cases, for which the signal-to-noise ratio is particularly low, we use a simple power-law model to fit the spectra [TBABS×ZTBABS×(ZPOW)].

The X-ray spectra of most (21/23) of the sources analysed here could be well reproduced by an SF model. For the two sources (NGC 2623 and ESO 060−IG16) that show a strong Fe K α line at 6.4 keV, or a clear excess over the SF model, we include an AGN component to account for the excess. This is done using the RXTORUS model, developed using the REFLEX ray-tracing platform (Paltani & Ricci 2017). The model assumes a toroidal absorber surrounding the accreting system. The inner-to-outer radius ratio of the torus is fixed to 0.5, while the inclination angle is fixed to 90° (i.e. corresponding to an edge-on scenario). In XSPEC, the model is: TBABS×ZTBABS×(ZPOW+APEC+ATABLE{RXTORUS_RPRC_200} +ETABLE{RXTORUS_CONT}*ZCUTOFFPL), where RXTORUS_RPRC_200 and RXTORUS_CONT are the reprocessed radiation and obscuration components, while ZCUTOFFPL is a cut-off power-law model used for the continuum. In the latter component, the cut-off energy is fixed to 200 keV (Ricci et al. 2018). The ZPOW component includes contributions from both star-forming regions and from scattered X-ray emission (e.g. Ueda et al. 2007, 2015; Ricci et al. 2017c; Gupta et al. 2021). The parameters obtained by our spectral analysis are reported in Table B1, while the column densities and intrinsic AGN luminosities, for all the objects in our sample, are reported in Table 2.

Details on the X-ray spectral analysis of the individual sources are reported in Appendix C. We verified whether the observed 2–10 keV luminosity is consistent with what would be expected by SF, considering the SFR of the galaxy. We used the L_{2-10}–SFR relations of Ranalli et al. (2003) and Lehmer et al. (2010), and found that all sources in which no AGNs were identified by our analysis have luminosities consistent, or lower, than the value expected from their SFR (see Fig. 2). The large fraction of U/LIRGs located below the relation of Ranalli et al. (2003) is consistent with the flattening reported by Torres-Albà et al. (2018) for a large sample of U/LIRGs observed by *Chandra*, and is possibly associated with an increasing level of obscuration within the star-forming regions (Torres-Albà et al. 2018).

Table 2. (1) *IRAS* name and (2) counterparts, observed (3) 2–10 keV and (4) 10–24 keV luminosities, intrinsic (5) 2–10 keV and (6) 10–24 keV AGN luminosities, (7) line-of-sight column densities towards the AGN, and (8) references. Luminosity upper limits are calculated based on the observed flux, and therefore could be significantly higher if the source is heavily obscured. A line-of-sight column density of $N_{\rm H} = 10^{24}$ cm^{-2} (10^{25} cm^{-2}) would correspond to an increase in luminosity of $\Delta[\log(L_{2-10}/{\rm erg\,s^{-1}})] = 1.3$ (2.8) and $\Delta[\log(L_{10-24}/{\rm erg\,s^{-1}})] = 0.4$ (1.9) in the 2–10 and 10–24 keV bands, respectively. The 2–10 keV AGN luminosity upper limit was extrapolated (assuming a power law with $\Gamma = 1.8$) from the upper limit on the 10–24 keV luminosity inferred by *NuSTAR*.

		Observed		Intrinsic (AGN)			
(1) *IRAS* name	(2) Source	(3) $\log L_{2-10}$ (erg s^{-1})	(4) $\log L_{10-24}$ (erg s^{-1})	(5) $\log L_{2-10}$ (erg s^{-1})	(6) $\log L_{10-24}$ (erg s^{-1})	(7) $\log N_{\rm H}$ (cm^{-2})	(8) Reference
F00085−1223	NGC 34	41.41	41.63	42.05	41.82	23.72 [23.62–23.81]	Ricci et al. (2017b)
F00163−1039	MCG−02−01−051	40.95	<40.52	<40.68	<40.52	–	Ricci et al. (2017b)
	MCG−02−01−052	40.21	<40.89	<41.05	<40.89	–	Ricci et al. (2017b)
F00344−3349	ESO 350−IG038	41.10	<40.44	<40.60	<40.44	–	This work
F00506+7248	MCG+12−02−001	40.66	<40.50	<40.66	<40.50	–	Ricci et al. (2017b)
F01053−1746	IC 1623A/B	41.33	40.95	<41.11	<40.95	–	This wok
F02069−1022	NGC 833	41.40	41.65	41.81	41.72	23.45 [23.40–23.49]	Oda et al. (2018)
	NGC 835	41.64	41.86	42.06	41.97	23.63 [23.52–23.76]	Oda et al. (2018)
F02401−0013	NGC 1068	41.19	41.39	43.11	42.95	≥24.99	Bauer et al. (2015)
F03117+4151	Mrk 1073	41.41	42.38	43.51	43.39	24.51 [24.34–24.56]	Yamada et al. (2020)
F03164+4119	NGC 1275	44.58	43.50	43.22	43.06	21.68 [21.62–21.78]	Ricci et al. (2017c)
F03316−3618	NGC 1365	41.71	41.79	42.00	41.84	23.30 [23.28–23.32]	Lanz et al. (2019)
F04454−4838	ESO 203−IG001	<41.38	<41.22	<41.38	<41.22	–	This work
F05054+1718	CGCG 468−002E	–	–	–	–	–	Ricci et al. (2017b)
	CGCG 468−002W	42.83	42.80	42.84	42.80	22.18 [22.15–22.20]	Ricci et al. (2017b)
F05189−2524	IRAS 05189−2524	43.10	43.30	43.57	43.02	23.10 [23.08–23.14]	Teng et al. (2015)
F06076−2139	South	41.36	41.90	42.34	42.18	23.79 [23.66–23.93]	Privon et al. (2020)
	North	40.83	–	–	–	–	Privon et al. (2020)
07251−0248	–	40.09	<41.87	<42.03	<41.87	–	This work
F08354+2555	NGC 2623	40.90	40.87	41.04	40.87	22.85 [22.63–23.08]	This work
F08520−6850	ESO 060−IG16	41.83	41.93	42.11	41.94	23.18 [22.95–23.40]	This work
F08572+3915	IRAS 08572+3915	41.06	<41.13	<41.29	<41.13	–	This work
IRAS F09111−1007	W	41.02	<41.36	<41.52	<41.36	–	This work
IRAS F09111−1007	E	41.16	<41.36	<41.52	<41.36	–	This work
F09320+6134	UGC 05101	41.77	42.83	43.43	43.23	24.11 [23.98–24.21]	Oda et al. (2017)
F09333+4841	MCG+08−18−013	40.80	<40.44	<40.60	<40.44	–	Ricci et al. (2017b)
	MCG+08−18−012	<40.64	<40.48	<40.64	<40.48	–	Ricci et al. (2017b)
F10015−0614	NGC 3110	40.59	<40.61	<40.77	<40.61	–	Ricci et al. (2017b)
	MCG−01−26−013	39.84	<40.27	<40.43	<40.27	–	Ricci et al. (2017b)
F10038−3338	IRAS F10038−3338	40.86	<40.81	<40.97	<40.81	–	This work
F10257−4339	NGC 3256	40.92	40.23	<40.39	<40.23	–	Lehmer et al. (2015)
F10565+2448	IRAS 10565+2448	41.31	<41.09	<41.25	<41.09	–	This work
F11257+5850	Arp 299W	41.22	41.30	43.18	42.98	24.54 [24.52 – NC]	Ptak et al. (2015)
	Arp 299E	41.01	–	–	–	–	Ptak et al. (2015)
F12043−3140	ESO 440−IG058N	40.41	<40.79	<40.95	<40.79	–	Ricci et al. (2017b)
	ESO 440−IG058S	40.22	<40.87	<41.03	<40.87	–	Ricci et al. (2017b)
F12112+0305	–	41.41	<41.73	<41.89	<41.73	–	This work
F12243−0036	NGC 4418	39.35	<39.49	<39.65	<39.49	–	This work
F12540+5708	Mrk 231	42.58	42.67	42.66	42.71	23.16 [23.08–23.25]	Teng et al. (2014)
F12590+2934	NGC 4922N	41.07	41.55	43.05	42.73	25.10 [24.63 – NC]	Ricci et al. (2017b)
	NGC 4922S	38.81	–	–	–	–	Ricci et al. (2017b)
13120−5453	IRAS 13120−5453	41.61	41.47	43.10	42.94	24.50 [24.27–24.74]	Teng et al. (2015)
F13126+2453	IC 860	38.55	<39.60	<39.76	<39.60	–	This work
F13188+0036	NGC 5104	40.24	<40.60	<40.76	<40.60	–	Privon et al. (2020)
F13197−1627	MCG−03−34−063	<40.13	<39.87	<40.13	<39.87	–	Ricci et al. (2017b)
	MCG−03−34−064	42.25	42.94	43.41	43.20	23.73 [23.72–23.74]	Ricci et al. (2017b)
F13229−2934	NGC 5135	41.20	42.06	43.35	43.19	24.80 [24.51–25.00]	Yamada et al. (2020)
F13362+4831	NGC 5256-NE	41.54	41.42	41.60	41.44	22.83 [22.48–23.03]	Iwasawa et al. (2020)
	NGC 5256-SW	41.08	41.73	43.13	42.97	>24.30	Iwasawa et al. (2020)
F13428+5608	Mrk 273	42.42	42.61	42.93	42.96	23.64 [23.58–23.73]	Teng et al. (2015)
F14348−1447	NE	41.13	<41.85	<42.01	<41.85	–	This work
	SW	41.54	<41.85	<42.01	<41.85	–	This work
F14378−3651	IRAS 14378−3651	41.34	<41.71	<41.87	<41.71	–	This work
F14544−4255	IC 4518A	42.40	42.70	42.85	42.75	23.38 [23.34–23.41]	Ricci et al. (2017b)
	IC 4518B	40.57	–	41.09	40.89	23.51 [23.26–23.86]	Ricci et al. (2017b)

Table 2 – *continued*

(1) *IRAS* name	(2) Source	Observed (3) $\log L_{2-10}$ (erg s^{-1})	Observed (4) $\log L_{10-24}$ (erg s^{-1})	Intrinsic (AGN) (5) $\log L_{2-10}$ (erg s^{-1})	Intrinsic (AGN) (6) $\log L_{10-24}$ (erg s^{-1})	(7) $\log N_{\rm H}$ (cm^{-2})	(8) Reference
F15250+3608	–	40.52	<41.66	<41.82	<41.66	–	This work
F15327+2340	Arp 220W	40.81	40.89	≳42.92	≳42.72	>24.72	Teng et al. (2015)
F16504+0228	NGC 6240 – North	42.03	42.42	43.30	43.17	24.19 [24.09–24.36]	Puccetti et al. (2016)
	NGC 6240 – South	42.38	42.86	43.72	43.58	24.17 [24.11–24.23]	Puccetti et al. (2016)
F16577+5900	NGC 6286	40.81	41.46	41.98	41.78	24.05 [23.85–24.34]	Ricci et al. (2016)
	NGC 6285	40.22	<40.35	<40.51	<40.35	–	Ricci et al. (2016)
F17138−1017	IRAS F17138−1017	41.00	<41.20	<41.36	<41.20	–	Ricci et al. (2017b)
F17207−0014	IRAS F17207−0014	41.41	<41.37	<41.53	<41.37	–	This work
F18293−3413	IRAS F18293−3413	41.02	<40.60	<40.76	<40.60	–	This work
F19297−0406	–	41.74	<42.01	<42.17	<42.01	–	This work
F20221−2458	NGC 6907	40.18	<40.22	<40.38	<40.22	–	Privon et al. (2020)
20264+2533	MCG +04−48−002	41.48	42.14	42.36	42.38	23.86 [23.79–23.92]	Ricci et al. (2017b)
	NGC 6921	41.28	42.22	42.97	42.72	24.15 [23.83–24.40]	Ricci et al. (2017b)
F20550+1655	CGCG 448−020W	39.46	<41.25	<41.41	<41.25	–	This work
	CGCG 448−020E	41.05	<41.25	<41.41	<41.25	–	This work
F20551−4250	ESO 286−IG19	41.65	<41.50	<41.66	<41.50	–	This work
F21453−3511	NGC 7130	41.11	41.88	43.05	42.62	24.61 [24.50–24.66]	Ricci et al. (2017b)
F23007+0836	NGC 7469	43.24	43.10	43.36	43.14	19.78 [19.60–19.90]	Ricci et al. (2017b)
	IC 5283	–	–	–	–	–	Ricci et al. (2017b)
F23128−5919	ESO 148−IG002	41.94	<41.23	<41.39	<41.23	–	This work
F23157+0618	NGC 7591	39.97	<40.26	<40.42	<40.26	–	Privon et al. (2020)
F23254+0830	NGC 7674	42.14	42.52	43.60	43.44	>24.48	Gandhi et al. (2017)
	NGC 7674A	–	–	–	–	–	Gandhi et al. (2017)
23262+0314	NGC 7679	41.60	41.50	41.60	41.50	<20.30	Ricci et al. (2017b)
	NGC 7682	41.28	42.28	43.70	43.30	24.39 [23.99–24.48]	Ricci et al. (2017b)
F23365+3604	–	41.48	<41.76	<41.92	<41.76	–	This work

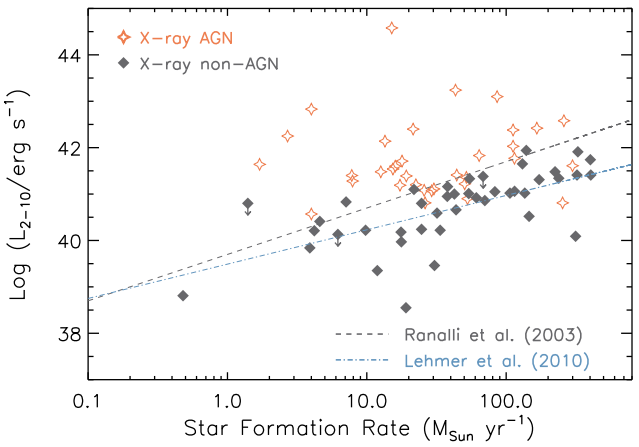

Figure 2. Observed 2–10 keV X-ray luminosities (see Table 2) versus SFR (see Table 1) for the sources of our sample divided into X-ray AGN (red empty stars) and X-ray non-AGN (black filled diamonds). The X-ray non-AGNs have 2–10 keV luminosities, consistent, or lower, than the values expected from their SFR (black continuous line, Ranalli, Comastri & Setti 2003; blue dot–dashed line, Lehmer et al. 2010), while X-ray AGNs are typically more luminous.

5 OBSCURATION AND X-RAY PROPERTIES OF AGN IN MERGERS

5.1 X-ray AGN

With the goal of understanding the evolution of AGN obscuration in the final phase of a galaxy merger, we report here the results obtained by studying 60 U/LIRGs from GOALS, effectively doubling the sample observed by *NuSTAR* presented by Ricci et al. (2017b; see Table 2). This was done including, besides the 23 sources presented here, the 30 objects reported in Ricci et al. (2017b), and several sources reported in recent literature (e.g. Iwasawa et al. 2020; Privon et al. 2020; Yamada et al. 2020). Using X-ray spectroscopy, we identify a total of 35 AGNs in these systems, 5 of which are associated with U/LIRGs in the *N* stage (i.e. showing no clear sign of interactions). In the following, we will refer to objects that were not identified as AGN in the X-rays, and for which only an upper limit of the AGN X-ray luminosity is reported in Table 2, as *X-ray non-AGN*.

The overall fraction of CT AGNs for the sample is 16/35 (46 ± 8 per cent[2]), while that of AGNs in merging galaxies is 13/30 (44^{+8}_{-9} per cent). This is significantly higher than what is inferred for the hard X-ray-selected *Swift*/BAT sample overall (27 ± 4 per cent; Ricci et al. 2015, 2017c), which is mostly composed of AGNs in isolated galaxies (Section 2.3). The sample of AGNs in U/LIRGs shows a larger fraction of both heavily obscured ($N_{\rm H} \geq 10^{23}$ cm^{-2}; 82^{+5}_{-7} per cent) and obscured ($N_{\rm H} \geq 10^{22}$ cm^{-2}; 90^{+4}_{-6} per cent) sources than the *Swift*/BAT sample (52 ± 4 per cent and 70 ± 5 per cent, respectively). This confirms the idea that the typical environment of these AGNs is different from that of AGNs in isolated galaxies, and that the obscuring medium almost fully covers the accreting SMBHs.

[2]Fractions are calculated following Cameron (2011), and the uncertainties quoted represent the 16th/84th quantiles of a binomial distribution, obtained using the Bayesian approach outlined in Cameron (2011).

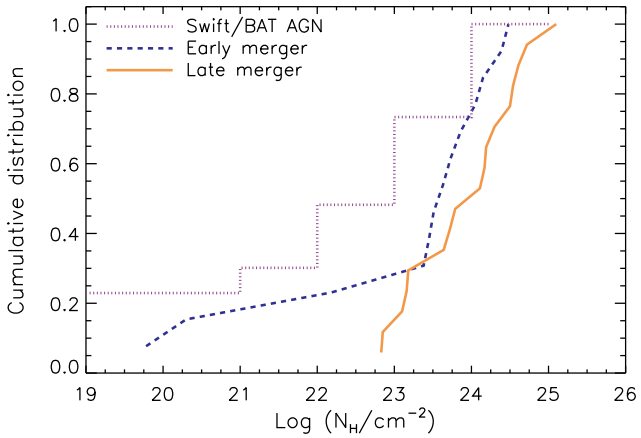

Figure 3. Column density cumulative distribution function for the AGN in our sample found in early (dashed blue line) and late mergers (continuous orange line). AGNs found in galaxies undergoing the final phases of a merger are more obscured than those in the early mergers, and than hard X-ray-selected nearby AGNs (dotted purple line; Ricci et al. 2015, 2017c).

5.2 AGN obscuration in the final phases of the merger

Dividing our sample into different merger stages, excluding the *N*-stage galaxies, we have 13 and 17 AGNs in early- and late-stage mergers, respectively. We find that 4/13 (33 ± 12 per cent) AGNs in early mergers (i.e. objects classified as being in *a* or *b* stages) are CT, a fraction in good agreement with what is found for the *Swift*/BAT sample. This shows that it takes time to build up the obscuration, since at the beginning of the merger the fraction of CT AGNs is not significantly higher than the comparison sample. A large fraction of these objects (10/13 or 74^{+11}_{-12} per cent) are heavily obscured, and almost all of them (11/13 or 81^{+9}_{-11} per cent) are obscured. AGNs in the late phases of the merger process (i.e. having *c* or *d* stages) show a higher fraction of CT AGNs (9/17 or 53^{+11}_{-12} per cent) than both hard X-ray-selected AGNs and AGNs in early-stage mergers. This is consistent with what was found by Ricci et al. (2017b), and Guainazzi et al. (2021) using *XMM–Newton*, who found that ∼47 per cent of the objects in their Sloan Digital Sky Survey optically selected sample are CT. Most of the AGNs in late-stage mergers are heavily obscured (15/17 or 85^{+7}_{-9} per cent), and all of them are obscured. The difference between early mergers, late mergers, and hard X-ray-selected AGNs is clearly illustrated in Fig. 3. AGNs in the final phases of the merger process are consistently more heavily obscured than hard X-ray-selected AGNs, and do not show the tail of objects (∼30 per cent) with $\log(N_{\rm H}/{\rm cm}^{-2}) \leq 23$ found in early mergers. Interestingly, 3/5 of the U/LIRGs in the *N* stage are CT (58^{+18}_{-19} per cent), and 4/5 (74^{+14}_{-19} per cent) are heavily obscured. This could be related to the fact that several of these systems are post-mergers.

Recent simulations (e.g. Blecha et al. 2018; Kawaguchi et al. 2020) have shown that the most obscured phase during the merger would correspond to small separation between the two nuclei. We divided our sample based on the projected nuclear separation, down to the scales in which two nuclei could be resolved at the distance of our sources ($d_{\rm sep} \sim 0.4$ kpc). In Fig. 4, we show the fraction of CT (top panel) and heavily obscured (bottom panel) AGNs versus the projected separation between the two galactic nuclei. We find that the CT fraction appears to peak when the two nuclei are at a projected distance of a few kpc (74^{+14}_{-19} per cent; $d_{\rm sep} \sim 0.4$–6 kpc), and that the fraction of heavily obscured sources is consistently higher than that found for *Swift*/BAT AGN, regardless of the projected nuclear separation. Similarly to the CT fraction, a peak in the

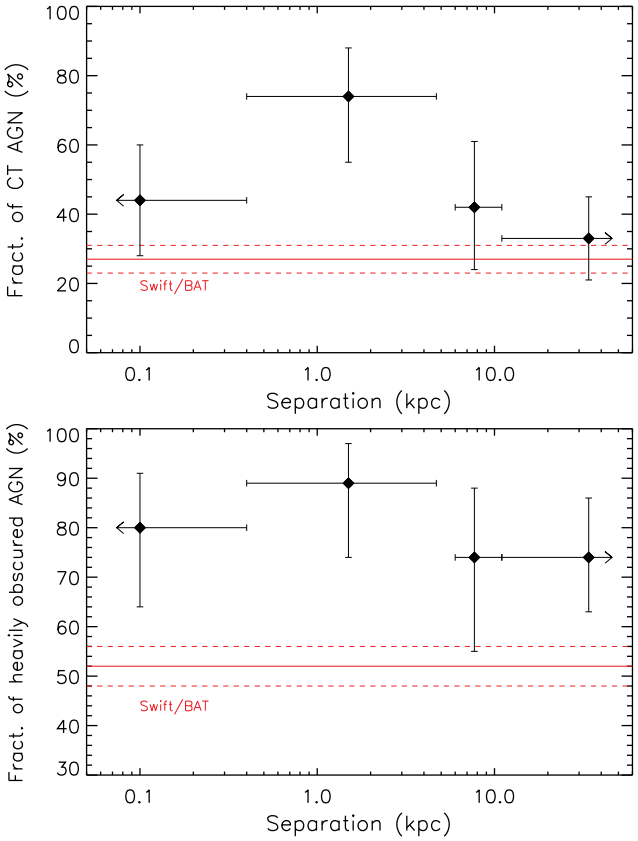

Figure 4. Fraction of CT ($N_{\rm H} \geq 10^{24}$ cm^{-2}; *top panel*) and heavily obscured ($N_{\rm H} \geq 10^{23}$ cm^{-2}; *bottom panel*) AGNs in our sample versus the projected separation between the two nuclei. The fraction of heavily obscured sources appears to be consistently higher than *Swift*/BAT AGN (red continuous line; Ricci et al. 2015, 2017c), and a tentative peak in the fraction of CT AGN is found at a separation of a few kpc. Fractions are calculated following Cameron (2011), and the uncertainties quoted represent the 16th/84th quantiles of a binomial distribution, obtained using the Bayesian approach outlined in Cameron (2011).

median $N_{\rm H}$ $[(1.6 \pm 0.5) \times 10^{24}$ cm$^{-2}]$ is also observed when the merging galaxies are at a few kpc distance (Fig. 5). The difference in the median column density with the *Swift*/BAT AGN sample (red continuous line) is particularly striking, with the X-ray-observed U/LIRGs having a median $N_{\rm H} \sim$ 1.5–2 orders of magnitude larger. It should be noted that our U/LIRGs are frequently interacting or merging galaxy pairs, a process that increases the amount of gas within the central ∼kpc (e.g. Di Matteo et al. 2007). This could lead to the GOALS galaxies having additional obscuration on hundreds of pc to kpc scales, compared to host galaxy obscuration seen in AGN in non-merging systems. The median CO luminosity of GOALS galaxies (2.6×10^9 K km s^{-1} pc^2; Herrero-Illana et al. 2019) is a factor of 7 higher than the CO luminosity of host galaxies of BAT AGN (4×10^8 K km s^{-1} pc^2, Koss et al. 2021). Different molecular gas masses could affect the contribution of host galaxy obscuration, but not up to the CT level (e.g. Buchner, Schulze & Bauer 2017). However, due to potential variations in the CO–H_2 conversion factor (e.g. Bolatto, Wolfire & Leroy 2013), it is unclear how different the total molecular gas masses are between the two samples.

5.3 IR and X-ray luminosities of AGN in U/LIRGs

In the left-hand panel of Fig. 6, we show the cumulative distribution of the IR luminosity of the X-ray-detected AGN in our sample,

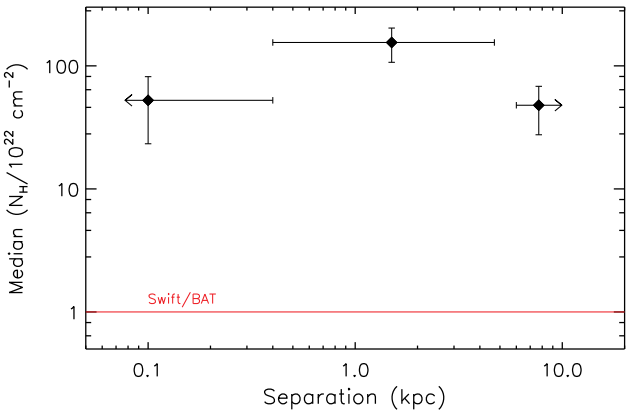

Figure 5. Median column density versus the separation between the two nuclei (Tables 1 and 2). AGNs in U/LIRGs tend to have significantly higher column densities than AGNs in nearby hard X-ray-selected AGN (red continuous line; Ricci et al. 2015, 2017c). Similarly to what was found for the fraction of CT AGNs (top panel of Fig. 4), we find a tentative peak of the column density for a projected nuclear separation of a few kpc. We conservatively considered the lower limit on N_H for the objects for which this parameter could not be constrained.

divided into Compton-thin (blue dashed line) and CT (red continuous line). The CT AGNs tend to have higher IR luminosities and, from performing a Kolmogorov–Smirnov (KS) test between the L_{IR} distributions of the two types of AGNs, we find a p-value of 0.01. This indicates that the IR luminosities of CT and Compton-thin AGNs are significantly different. Interestingly, CT AGNs (red filled circles in the right-hand panel of Fig. 6) are mostly found to have higher intrinsic X-ray luminosities than Compton-thin sources (empty red stars), and only one of them is found to have $L_{2-10} \lesssim 10^{43}$ erg s^{-1}. A KS test between the two luminosity distributions results in a p-value of 4.6×10^{-4}. While we cannot exclude that this is an evolutionary effect, where more obscured sources accrete more rapidly because they have more gas available in their surroundings, it is possible that this is related to a selection effect. In fact, even with our sensitive *NuSTAR* hard X-ray observations, because of the strong depletion of the X-ray flux at $N_H > 10^{24}$ cm^{-2}, it would be difficult to detect a large number of low-luminosity heavily obscured AGNs. This is particularly true if the heavily obscuring material covers most of the X-ray sources, as suggested by the very large fraction of heavily obscured sources (see also Ricci et al. 2017b), which would lead to a small fraction of the X-ray radiation reprocessed by the circumnuclear environment being able to escape the system.

5.4 Constraints on obscuration from IR-identified AGN

Multiwavelength tracers of AGN activity can help discover heavily obscured accreting SMBHs that cannot be identified in the X-rays. In a companion paper (Ricci et al. in preparation), we discuss in more detail these proxies of AGN activity for our sample of U/LIRGs, comparing them with the AGN X-ray emission. Considering [Ne V] as a good tracer of AGN activity (e.g. Weedman et al. 2005; Armus et al. 2006; Goulding & Alexander 2009; Petric et al. 2011), we can identify only one accreting SMBH (in the late-stage merger IRAS F23128−5919) that is not an X-ray-detected AGN. Assuming that the [Ne V] 14.32 μm emission is entirely due to the AGN, and invoking the [Ne V]/X-ray correlation from Satyapal et al. (2007), we would expect this source to have a bolometric AGN luminosity of 6×10^{44} erg s^{-1}. Using a 2–10 keV bolometric correction of $\kappa_X =$ 20 (e.g. Vasudevan & Fabian 2007), the source would need to be obscured by $N_H \gtrsim 1.9 \times 10^{24}$ cm^{-2} to have a 2–10 keV AGN luminosity consistent with the upper limit inferred by our study (Table 2), which is reasonable given the N_H distribution of the other AGN.

Considering MIR photometry, and assuming a $W1 - W2 > 0.8$ threshold for AGN activity (Stern et al. 2012), we find 13 sources that are classified as AGN with *WISE* (including IRAS F23128−5919), but were not identified by our broad-band X-ray analysis. Of these, 11 are in the final stages (*c* and *d*) of the merger process, one is not a merger (*N*), and another is stage *b*. This would be even further evidence for the CT nature of most late-stage mergers. We use the method outlined by Pfeifle et al. (2021; see their equation 2), assuming that the 12 μm emission is dominated by the AGN in these sources, to get constraints on the N_H needed for these sources to remain undetected by *NuSTAR*. We find that all the lower limits on the column density are above $\sim 3 \times 10^{24}$ cm^{-2}. Including these lower limits to our sample, a total of 69^{+8}_{-9} per cent of the AGNs in the final stages of mergers would be CT. Dividing this sample according to the nuclear separation, we find that the peak of the CT fraction would again be found at ∼0.4−6 kpc (85^{+8}_{-12} per cent), while 62^{+13}_{-14} per cent of the AGNs in merging galaxies that show a single galactic nucleus would be CT. It should be noted that, considering these candidate AGNs, we are still able to detect with *NuSTAR* the accreting SMBHs that are contributing to most of the overall IR emission. Using the 12 μm AGN emission for the *WISE*-selected candidate AGNs that were not detected in the X-rays, considering a typical AGN IR spectrum (Stalevski et al. 2012, 2016), we find that accreting SMBHs would in fact contribute at most ∼40 per cent to the IR flux.

5.5 The evolution of obscuration in U/LIRGs

This work and recent X-ray studies (e.g. Ricci et al. 2017b) show that the obscuration properties of AGN in U/LIRGs are very different from those of AGN in isolated galaxies. In particular, AGNs in late mergers are fully embedded in gas with $N_H \geq 10^{23}$ cm^{-2}. The most extreme of these sources could be associated with Compact Obscured Nuclei (or CONs; Aalto et al. 2015, 2019; Falstad et al. 2021), galaxies that show strong and compact vibrationally excited HCN from their nuclear regions. This emission is created by a strong 14 μm continuum, which could be due to strong emission from a heavily obscured AGN. The presence of obscuring material with a very high covering factor around AGN in galaxies undergoing the final phases of a merger has also been confirmed by a recent study focusing on the [O IV] 25.89 μm line. Yamada et al. (2019) found that the ratio between the [O IV] and the 12 μm AGN luminosity decreases as the merger progresses, which suggests that the covering factor of the material tends to be larger in late-stage mergers. Ricci et al. (2017d) demonstrated that, due to the presence of dusty gas (e.g. Fabian, Celotti & Erlund 2006; Fabian, Vasudevan & Gandhi 2008), radiation pressure can be very effective in reducing the covering factor of the obscuring material, by removing gas from the environment of nearby AGN already at low Eddington ratios (i.e. $\lambda_{Edd} \sim 10^{-2}$; see also García-Burillo et al. 2021). This process might not be as effective in mergers, where the obscuring material might be located at hundreds of parsecs from the accreting source (and therefore outside the sphere of influence of the SMBH). In these objects, the AGN would need to attain high luminosities (and considerably higher Eddington ratios) in order to remove the obscuring material (Ricci et al. 2017d; Jun et al. 2021). This might happen in the final stages of the merger process, when the accretion rate of the SMBH is expected to reach

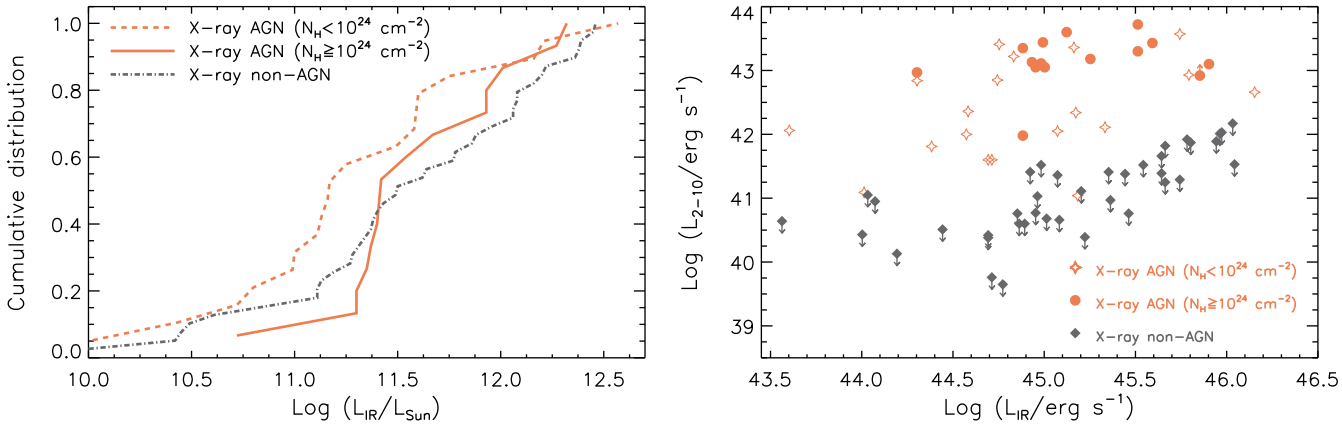

Figure 6. Left-hand panel: Cumulative distribution function of the 8–1000 μm IR luminosities of X-ray non-AGNs (grey dot–dashed line) and Compton-thin (red dashed line) and CT (red continuous line) AGNs, showing that CT AGNs are typically found in systems that are more luminous in the IR. Right-hand panel: Intrinsic 2–10 keV luminosity versus 8–1000 μm luminosity of the X-ray-detected Compton-thin (red empty stars) and CT (red filled circles) AGNs in our sample. The plot also shows the upper limit on the 2–10 keV luminosity of the sources for which an AGN was not identified in the X-rays (grey filled diamonds). These upper limits are calculated based on the observed flux, and therefore could be significantly higher if the source is heavily obscured. A line-of-sight column density of $N_{\rm H} = 10^{24}\,{\rm cm}^{-2}$ ($10^{25}\,{\rm cm}^{-2}$) would correspond to an increase in luminosity of $\Delta[\log(L_{2-10}/{\rm erg\,s}^{-1})] = 1.3$ (2.8). The figure illustrates that the CT AGNs we identify typically have higher intrinsic X-ray luminosities than the Compton-thin AGNs.

very high levels (e.g. Blecha et al. 2018; Kawaguchi et al. 2020), and it could be the cause of the tentative decrease at $d_{\rm sep} \lesssim 0.4$ kpc we observe both in the fraction of CT AGNs (top panel of Fig. 4) and in the median $N_{\rm H}$ (Fig. 5). Alternatively, the decrease could be due to sources being more heavily obscured in the final phases of the merger process, which would lead us to detect preferentially the least obscured AGN.

6 SUMMARY AND CONCLUSIONS

In this work, we have studied broad-band X-ray observations of 60 nearby U/LIRGs from the GOALS sample to understand the link between AGN obscuration and galaxy mergers. A total of 35 X-ray-detected AGNs are identified in these systems, 30 of which reside in merging galaxies. We find that

(i) The U/LIRGs in our sample show a higher fraction of heavily obscured ($N_{\rm H} \geq 10^{23}\,{\rm cm}^{-2}$; 82^{+5}_{-7} per cent) and CT AGNs ($N_{\rm H} \geq 10^{24}\,{\rm cm}^{-2}$; 46 ± 8 per cent) than local hard X-ray-selected AGNs (52 ± 4 per cent and 27 ± 4 per cent, respectively; Ricci et al. 2015, 2017c; see Fig. 3). The median line-of-sight column density towards AGN in U/LIRGs is also ∼1.5–2 orders of magnitude larger than that of hard X-ray-selected AGN (Fig. 5).

(ii) Roughly half (53^{+11}_{-12} per cent) of the AGNs in galaxies undergoing the final stages of mergers are CT. This fraction of CT sources is higher than that found in AGNs in early mergers (33 ± 12 per cent) and in local hard X-ray-selected AGNs. Considering the X-ray non-detections of objects that are identified as AGN in the IR (Section 5.4), the fraction of CT AGNs in late-stage mergers value would be higher (69^{+8}_{-9} per cent).

(iii) A tentative peak in the fraction of CT AGNs is found at nuclear projected separations of $d_{\rm sep} \sim 0.4$–6 kpc (74^{+14}_{-19} per cent; top panel of Fig. 4). The median line-of-sight column density is also found to peak [$(1.6 \pm 0.5) \times 10^{24}\,{\rm cm}^{-2}$] for a similar range of nuclear separations (Fig. 5). Considering the X-ray non-detection of objects that are identified as AGN in the IR, the CT fraction at $d_{\rm sep} \sim$ 0.4–6 kpc would be 85^{+8}_{-12} per cent. The possible decrease at $d_{\rm sep} \lesssim$ 0.4 kpc both in the fraction of CT AGNs and in the median $N_{\rm H}$ could be related to the effect of radiation pressure or to the fact that sources are more heavily obscured in the final phases of the merger process, and therefore we would detect preferentially the least obscured AGN.

(iv) The vast majority (85^{+7}_{-9} per cent) of the AGNs in late-stage mergers are heavily obscured. This fraction is consistent with that obtained for early mergers (74^{+11}_{-12} per cent), while it is significantly higher than for local hard X-ray-selected AGNs.

(v) CT AGNs typically have higher intrinsic (i.e. absorption-corrected) X-ray luminosities than less obscured sources. This could be either due to an evolutionary effect, with more obscured sources accreting more rapidly because they have more gas available in their surroundings, or to a selection effect. In the latter scenario, our *NuSTAR* observations might be unable to detect a significant fraction of heavily obscured less luminous ($L_{2-10} \lesssim 10^{43}\,{\rm erg\,s}^{-1}$) AGNs, while detecting most of the AGNs that contribute significantly to the energetics of these U/LIRGs (Ricci et al., in preparation).

Our work confirms the idea that the close environments of AGNs in U/LIRGs undergoing the final stages of the merger process are different from those of AGNs in isolated galaxies (e.g. Ricci et al. 2017b), with the former having an accreting source completely buried by obscuring material. We speculate that, due to the high density and large covering factor of the obscuring dust and gas, there might be an important fraction of lower luminosity ($L_{2-10} \lesssim 10^{43}\,{\rm erg\,s}^{-1}$) AGNs that we are still missing in late mergers. Extremely sensitive hard X-ray telescopes, such as those onboard the proposed missions *FORCE* (Mori et al. 2016; Nakazawa et al. 2018) and *HEX-P* (Madsen et al. 2018), would be fundamental to shed light on the accretion properties of SMBHs in these nearby systems. The strong nuclear obscuration associated with AGN in mergers, combined with the increase of galaxies in mergers with redshift (e.g. Le Fèvre et al. 2000; Conselice, Yang & Bluck 2009; Lotz et al. 2011), might contribute to the observed positive relation between the fraction of obscured sources and redshift (e.g. La Franca et al. 2005; Treister & Urry 2006; Ueda et al. 2014; Buchner et al. 2015). *Athena* (Nandra et al. 2013) will be a fundamental tool to assess the role of mergers in the increase of the fraction of obscured AGNs with redshift, shedding light on the properties of accreting SMBHs at $z \gtrsim 1$.

ACKNOWLEDGEMENTS

We thank the referee for their useful suggestions, which helped us in improving the quality of the manuscript. We thank Chin-Shin Chang for useful comments on the manuscript. LCH was supported by the National Key Research and Development Program of China (2016YFA0400702) and the National Science Foundation of China (11721303 and 11991052). CR acknowledges support from the Fondecyt Iniciacion grant 11190831. ET acknowledges support from CATA-Basal AFB-170002, FONDECYT Regular grant 1190818, ANID Anillo ACT172033, and Millennium Nucleus NCN19_058 (TITANs). FEB acknowledges support from ANID – Millennium Science Initiative Program – ICN12_009, CATA-Basal – AFB-170002, and FONDECYT Regular – 1190818 and 1200495. SA gratefully acknowledges funding from the European Research Council (ERC) under the European Union's Horizon 2020 research and innovation programme (grant agreement No 789410). VU acknowledges funding support from NASA Astrophysics Data Analysis Program (ADAP) Grant 80NSSC20K0450. AMM acknowledges support from the National Science Foundation under grant number 2009416. KI acknowledges support by the Spanish MICINN under grant Proyecto/AEI/10.13039/501100011033 and 'Unit of excellence María de Maeztu 2020-2023' awarded to ICCUB (CEX2019-000918-M). PA acknowledges financial support from ANID Millennium Nucleus NCN19-058 (TITANS) and the Max Planck Society through a Partner Group. HI acknowledges support from JSPS KAKENHI Grant Number JP19K23462. This work made use of data from the *NuSTAR* mission, a project led by the California Institute of Technology, managed by the Jet Propulsion Laboratory, and funded by the National Aeronautics and Space Administration. We thank the *NuSTAR* Operations, Software and Calibration teams for support with the execution and analysis of these observations. This research has made use of the *NuSTAR* Data Analysis Software (NUSTARDAS) jointly developed by the ASI Science Data Center (ASDC, Italy) and the California Institute of Technology (Caltech, USA), and of the NASA/IPAC Infrared Science Archive and NASA/IPAC Extragalactic Database (NED), which are operated by the Jet Propulsion Laboratory, California Institute of Technology, under contract with the National Aeronautics and Space Administration.

DATA AVAILABILITY

The data sets generated and/or analysed in this study are available from the corresponding author on reasonable request.

REFERENCES

Aalto S. et al., 2015, A&A, 584, A42
Aalto S. et al., 2019, A&A, 627, A147
Alonso-Herrero A., Pereira-Santaella M., Rieke G. H., Rigopoulou D., 2012, ApJ, 744, 2
Alonso-Herrero A., Rieke G. H., Rieke M. J., Colina L., Pérez-González P. G., Ryder S. D., 2006, ApJ, 650, 835
Alonso-Herrero A., Rieke G. H., Rieke M. J., Scoville N. Z., 2000, ApJ, 532, 845
Annuar A. et al., 2015, ApJ, 815, 36
Armus L. et al., 2006, ApJ, 640, 204
Armus L. et al., 2007, ApJ, 656, 148
Armus L. et al., 2009, PASP, 121, 559
Armus L., Charmandaris V., Soifer B. T., 2020, Nat. Astron., 4, 467
Armus L., Heckman T., Miley G., 1987, AJ, 94, 831
Assef R. J. et al., 2015, ApJ, 804, 27
Barnes J. E., Hernquist L. E., 1991, ApJ, 370, L65
Bauer F. E. et al., 2015, ApJ, 812, 116
Baumgartner W. H., Tueller J., Markwardt C. B., Skinner G. K., Barthelmy S., Mushotzky R. F., Evans P. A., Gehrels N., 2013, ApJS, 207, 19
Bitsakis T., Charmandaris V., Appleton P. N., Díaz-Santos T., Le Floc'h E., da Cunha E., Alatalo K., Cluver M., 2014, A&A, 565, A25
Blecha L., Snyder G. F., Satyapal S., Ellison S. L., 2018, MNRAS, 478, 3056
Blumenthal K. A., Barnes J. E., 2018, MNRAS, 479, 3952
Bolatto A. D., Wolfire M., Leroy A. K., 2013, ARA&A, 51, 207
Buchner J. et al., 2015, ApJ, 802, 89
Buchner J., Schulze S., Bauer F. E., 2017, MNRAS, 464, 4545
Burlon D., Ajello M., Greiner J., Comastri A., Merloni A., Gehrels N., 2011, ApJ, 728, 58
Cameron E., 2011, Publ. Astron. Soc. Aust., 28, 128
Clements D. L., Sutherland W. J., McMahon R. G., Saunders W., 1996, MNRAS, 279, 477
Conselice C. J., Yang C., Bluck A. F. L., 2009, MNRAS, 394, 1956
De Rosa A. et al., 2019, New Astron. Rev., 86, 101525
Del Moro A. et al., 2016, MNRAS, 456, 2105
Di Matteo P., Combes F., Melchior A.-L., Semelin B., 2007, A&A, 468, 61
Di Matteo T., Springel V., Hernquist L., 2005, Nature, 433, 604
Díaz-Santos T. et al., 2011, ApJ, 741, 32
Díaz-Santos T. et al., 2017, ApJ, 846, 32
Donley J. L. et al., 2018, ApJ, 853, 63
Dutta D. et al., 2019, MNRAS, 489, 1099
Dutta D., et al., 2018, MNRAS, 480, 947
Ellison S. L., Mendel J. T., Patton D. R., Scudder J. M., 2013, MNRAS, 435, 3627
Ellison S. L., Patton D. R., Mendel J. T., Scudder J. M., 2011, MNRAS, 418, 2043
Ellison S. L., Patton D. R., Simard L., McConnachie A. W., 2008, AJ, 135, 1877
Ellison S. L., Viswanathan A., Patton D. R., Bottrell C., McConnachie A. W., Gwyn S., Cuillandre J.-C., 2019, MNRAS, 487, 2491
Fabian A. C., Celotti A., Erlund M. C., 2006, MNRAS, 373, L16
Fabian A. C., Vasudevan R. V., Gandhi P., 2008, MNRAS, 385, L43
Falstad N. et al., 2021, A&A, 649, A105
Fan L. et al., 2016, ApJ, 822, L32
Ferrarese L., Merritt D., 2000, ApJ, 539, L9
Foord A., Gültekin K., Runnoe J. C., Koss M. J., 2021, ApJ, 907, 72
Franceschini A. et al., 2003, MNRAS, 343, 1181
Gabriel C. et al., 2004, in Ochsenbein F., Allen M. G., Egret D., eds, ASP Conf. Ser. Vol. 314, Astronomical Data Analysis Software and Systems (ADASS) XIII. Astron. Soc. Pac., San Francisco, p. 759
Gandhi P. et al., 2017, MNRAS, 467, 4606
García-Burillo S. et al., 2021, preprint (arXiv:2104.10227)
Garmire G. P., Bautz M. W., Ford P. G., Nousek J. A., Ricker G. R., Jr., 2003, in Truemper J. E., Tananbaum H. D., eds, Proc. SPIE Conf. Ser. Vol. 4851, X-Ray and Gamma-Ray Telescopes and Instruments for Astronomy. SPIE, Bellingham, p. 28
Garofali K. et al., 2020, ApJ, 903, 79
Gebhardt K. et al., 2000, ApJ, 539, L13
Glikman E., Simmons B., Mailly M., Schawinski K., Urry C. M., Lacy M., 2015, ApJ, 806, 218
Goulding A. D. et al., 2018, PASJ, 70, S37
Goulding A. D., Alexander D. M., 2009, MNRAS, 398, 1165
Guainazzi M. et al., 2021, MNRAS, 504, 393
Gupta K. K. et al., 2021, MNRAS, 504, 428
Haan S. et al., 2011, AJ, 141, 100
Harrison F. A. et al., 2013, ApJ, 770, 103
Herrero-Illana R. et al., 2019, A&A, 628, A71
Hickox R. C., Alexander D. M., 2018, ARA&A, 56, 625
Hickson P., 1982, ApJ, 255, 382
Hong J., Im M., Kim M., Ho L. C., 2015, ApJ, 804, 34
Hopkins P. F., Hernquist L., Cox T. J., Kereš D., 2008, ApJS, 175, 356
Hou M., Li Z., Liu X., 2020, ApJ, 900, 79
Howell J. H. et al., 2010, ApJ, 715, 572

Ichikawa K. et al., 2019, ApJ, 870, 31
Ichikawa K., Ricci C., Ueda Y., Matsuoka K., Toba Y., Kawamuro T., Trakhtenbrot B., Koss M. J., 2017, ApJ, 835, 74
Imanishi M., 2002, ApJ, 569, 44
Imanishi M., Dudley C. C., 2000, ApJ, 545, 701
Imanishi M., Dudley C. C., Maiolino R., Maloney P. R., Nakagawa T., Risaliti G., 2007, ApJS, 171, 72
Imanishi M., Dudley C. C., Maloney P. R., 2006, ApJ, 637, 114
Inami H. et al., 2010, AJ, 140, 63
Inami H. et al., 2013, ApJ, 777, 156
Inami H. et al., 2018, A&A, 617, A130
Iwasawa K. et al., 2011, A&A, 529, A106
Iwasawa K. et al., 2020, A&A, 640, A95
Iwasawa K., Sanders D. B., Evans A. S., Mazzarella J. M., Armus L., Surace J. A., 2009, ApJ, 695, L103
Jansen F. et al., 2001, A&A, 365, L1
Joseph R. D., Wright G. S., 1985, MNRAS, 214, 87
Jun H. D., Assef R. J., Carroll C. M., Hickox R. C., Kim Y., Lee J., Ricci C., Stern D., 2021, ApJ, 906, 21
Kalberla P. M. W., Burton W. B., Hartmann D., Arnal E. M., Bajaja E., Morras R., Pöppel W. G. L., 2005, A&A, 440, 775
Kawaguchi T., Yutani N., Wada K., 2020, ApJ, 890, 125
Kocevski D. D. et al., 2012, ApJ, 744, 148
Kocevski D. D. et al., 2015, ApJ, 814, 104
Kormendy J., Ho L. C., 2013, ARA&A, 51, 511
Koss M. J. et al., 2016a, ApJ, 825, 85
Koss M. J. et al., 2016b, ApJ, 824, L4
Koss M. J. et al., 2018, Nature, 563, 214
Koss M. J. et al., 2021, ApJS, 252, 29
Koss M., Mushotzky R., Baumgartner W., Veilleux S., Tueller J., Markwardt C., Casey C. M., 2013, ApJ, 765, L26
Koss M., Mushotzky R., Treister E., Veilleux S., Vasudevan R., Trippe M., 2012, ApJ, 746, L22
Koss M., Mushotzky R., Veilleux S., Winter L. M., Baumgartner W., Tueller J., Gehrels N., Valencic L., 2011, ApJ, 739, 57
Koss M., Mushotzky R., Veilleux S., Winter L., 2010, ApJ, 716, L125
Kraft R. P., Burrows D. N., Nousek J. A., 1991, ApJ, 374, 344
La Franca F. et al., 2005, ApJ, 635, 864
LaMassa S. M. et al., 2016, ApJ, 820, 70
Lansbury G. B. et al., 2017, ApJ, 836, 99
Lanz L. et al., 2019, ApJ, 870, 26
Lanzuisi G. et al., 2015, A&A, 573, A137
Le Fèvre O. et al., 2000, MNRAS, 311, 565
Lehmer B. D. et al., 2015, ApJ, 806, 126
Lehmer B. D., Alexander D. M., Bauer F. E., Brandt W. N., Goulding A. D., Jenkins L. P., Ptak A., Roberts T. P., 2010, ApJ, 724, 559
Lonsdale C. J., Persson S. E., Matthews K., 1984, ApJ, 287, 95
Lotz J. M., Jonsson P., Cox T. J., Croton D., Primack J. R., Somerville R. S., Stewart K., 2011, ApJ, 742, 103
Lu N. et al., 2017, ApJS, 230, 1
Madsen K. K. et al., 2015, ApJS, 220, 8
Madsen K. K. et al., 2018, in den Herder J.-W. A., Nikzad S., Nakazawa K., eds, Proc. SPIE Conf. Ser. Vol. 10699, Space Telescopes and Instrumentation 2018: Ultraviolet to Gamma Ray. SPIE, Bellingham, p. 106996M
Magorrian J. et al., 1998, AJ, 115, 2285
Medling A. M. et al., 2014, ApJ, 784, 70
Mihos J. C., Hernquist L., 1996, ApJ, 464, 641
Mori K. et al., 2016, in den Herder J.-W. A., Takahashi T., Bautz M., eds, Proc. SPIE Conf. Ser. Vol. 9905, Space Telescopes and Instrumentation 2016: Ultraviolet to Gamma Ray. SPIE, Bellingham, p. 99051O
Murphy E. J. et al., 2011, ApJ, 737, 67
Nakazawa K. et al., 2018, in den Herder J.-W. A., Nikzad S., Nakazawa K., eds, Proc. SPIE Conf. Ser. Vol. 10699, Space Telescopes and Instrumentation 2018: Ultraviolet to Gamma Ray. SPIE, Bellingham, p. 106992D
Nandra K. et al., 2013, preprint (arXiv:1306.2307)
Nardini E., Risaliti G., 2011, MNRAS, 415, 619
Nardini E., Risaliti G., Watabe Y., Salvati M., Sani E., 2010, MNRAS, 405, 2505
O'Sullivan E. et al., 2014, ApJ, 793, 73
Oda S., Tanimoto A., Ueda Y., Imanishi M., Terashima Y., Ricci C., 2017, ApJ, 835, 179
Oda S., Ueda Y., Tanimoto A., Ricci C., 2018, ApJ, 855, 79
Paltani S., Ricci C., 2017, A&A, 607, A31
Pereira-Santaella M. et al., 2011, A&A, 535, A93
Pérez-Torres M., Mattila S., Alonso-Herrero A., Aalto S., Efstathiou A., 2021, A&AR, 29, 2
Petric A. O. et al., 2011, ApJ, 730, 28
Pfeifle R. W. et al., 2019a, ApJ, 883, 167
Pfeifle R. W. et al., 2019b, ApJ, 875, 117
Pfeifle R. W. et al., 2021, preprint (arXiv:2102.04412)
Piconcelli E. et al., 2015, A&A, 574, L9
Privon G. C. et al., 2020, ApJ, 893, 149
Ptak A. et al., 2015, ApJ, 800, 104
Puccetti S. et al., 2016, A&A, 585, A157
Ramos Almeida C., Ricci C., 2017, Nat. Astron., 1, 679
Ranalli P., Comastri A., Setti G., 2003, A&A, 399, 39
Ricci C. et al., 2016, ApJ, 819, 4
Ricci C. et al., 2017a, ApJ, 835, 105
Ricci C. et al., 2017b, MNRAS, 468, 1273
Ricci C. et al., 2017c, ApJS, 233, 17
Ricci C. et al., 2017d, Nature, 549, 488
Ricci C. et al., 2018, MNRAS, 480, 1819
Ricci C., Ueda Y., Koss M. J., Trakhtenbrot B., Bauer F. E., Gandhi P., 2015, ApJ, 815, L13
Sanders D. B., Mazzarella J. M., Kim D.-C., Surace J. A., Soifer B. T., 2003, AJ, 126, 1607
Sanders D. B., Mirabel I. F., 1996, ARA&A, 34, 749
Sanders D. B., Soifer B. T., Elias J. H., Madore B. F., Matthews K., Neugebauer G., Scoville N. Z., 1988, ApJ, 325, 74
Satyapal S. et al., 2017, ApJ, 848, 126
Satyapal S., Ellison S. L., McAlpine W., Hickox R. C., Patton D. R., Mendel J. T., 2014, MNRAS, 441, 1297
Satyapal S., Vega D., Heckman T., O'Halloran B., Dudik R., 2007, ApJ, 663, L9
Schawinski K., Simmons B. D., Urry C. M., Treister E., Glikman E., 2012, MNRAS, 425, L61
Secrest N. J., Ellison S. L., Satyapal S., Blecha L., 2020, MNRAS, 499, 2380
Shangguan J., Ho L. C., Li R., Zhuang M.-Y., Xie Y., Li Z., 2019, ApJ, 870, 104
Silverman J. D. et al., 2011, ApJ, 743, 2
Stalevski M., Fritz J., Baes M., Nakos T., Popović L. Č., 2012, MNRAS, 420, 2756
Stalevski M., Ricci C., Ueda Y., Lira P., Fritz J., Baes M., 2016, MNRAS, 458, 2288
Stern D. et al., 2012, ApJ, 753, 30
Stierwalt S. et al., 2013, ApJS, 206, 1
Stierwalt S. et al., 2014, ApJ, 790, 124
Strüder L. et al., 2001, A&A, 365, L18
Teng S. H. et al., 2014, ApJ, 785, 19
Teng S. H. et al., 2015, ApJ, 814, 56
Teng S., Veilleux S., 2010, ApJ, 725, 1848
Toba Y. et al., 2020, ApJ, 888, 8
Torres-Albà N. et al., 2018, A&A, 620, A140
Treister E., Schawinski K., Urry C. M., Simmons B. D., 2012, ApJ, 758, L39
Treister E., Urry C. M., 2006, ApJ, 652, L79
U V. et al., 2012, ApJS, 203, 9
U V. et al., 2019, ApJ, 871, 166
Ueda Y. et al., 2007, ApJ, 664, L79
Ueda Y. et al., 2015, ApJ, 815, 1
Ueda Y., Akiyama M., Hasinger G., Miyaji T., Watson M. G., 2014, ApJ, 786, 104
Urrutia T., Lacy M., Becker R. H., 2008, ApJ, 674, 80
Vasudevan R. V., Fabian A. C., 2007, MNRAS, 381, 1235

Veilleux S. et al., 2009, ApJS, 182, 628
Veilleux S., Kim D.-C., Sanders D. B., 1999, ApJ, 522, 113
Veilleux S., Kim D.-C., Sanders D. B., Mazzarella J. M., Soifer B. T., 1995, ApJS, 98, 171
Weedman D. W. et al., 2005, ApJ, 633, 706
Weisskopf M. C., Tananbaum H. D., Van Speybroeck L. P., O'Dell S. L., 2000, in Truemper J. E., Aschenbach B., eds, Proc. SPIE Conf. Ser. Vol. 4012, X-Ray Optics, Instruments, and Missions III. SPIE, Bellingham, p. 2
White S. D. M., Rees M. J., 1978, MNRAS, 183, 341
Wilms J., Allen A., McCray R., 2000, ApJ, 542, 914
Wu J. et al., 2012, ApJ, 756, 96
Yamada S., Ueda Y., Tanimoto A., Kawamuro T., Imanishi M., Toba Y., 2019, ApJ, 876, 96
Yamada S., Ueda Y., Tanimoto A., Oda S., Imanishi M., Toba Y., Ricci C., 2020, ApJ, 897, 107
Yamada S. et al., 2021, preprint(arXiv:210710855Y)
Zappacosta L. et al., 2018, A&A, 618, A28

APPENDIX A: X-RAY OBSERVATION LOG

In Table A1, we report the X-ray observations used in our study. Details on the data reduction can be found in Section 3.

Table A1. X-ray observation log. The table reports the name of the *IRAS* source and of the counterparts (columns 1 and 2, respectively), as well the X-ray observatory used (3), the ID (4), date (5), and exposure (6) of the observation.

(1) *IRAS* name	(2) Source	(3) Observatory	(4) Obs. ID	(5) Date	(6) Exposure (ks)
F00344−3349	ESO 350−IG038	*NuSTAR*	60374008002	2018-01-15	22.6
		Chandra	8175	2006-10-28	54.0
F01053−1746	IC 1623A and IC 1623B	*NuSTAR*	50401001002	2019-01-19	20.6
		Chandra	7063	2005-10-20	59.4
		XMM–Newton	0830440101	2019-01-10	22.6
F04454−4838	ESO 203−IG001	*NuSTAR*	60374001002	2018-05-25	21.1
		Chandra	7802	2008-01-17	15.0
07251−0248		*NuSTAR*	60667003002	2021-04-09	32.6
		Chandra	7804	2006-12-01	15.6
F08354+2555	NGC 2623	*NuSTAR*	60374010002	2018-05-24	38.7
		Chandra	4059	2003-01-03	19.8
		XMM–Newton	0025540301	2001-04-27	4.9
F08520−6850	ESO 060−IG16 (NE and SW)	*NuSTAR*	60101053002	2015-12-01	41.8
		Chandra	7888	2007-05-31	14.7
F08572+3915	NW and SE	*NuSTAR*	50401004002	2019-04-04	211.3
		NuSTAR	60001088002	2013-05-23	24.1
		Chandra	6862	2006-01-26	15.1
		XMM–Newton	0830420101	2019-04-05	63.5
		XMM–Newton	0830420101	2019-04-07	63.5
F09111−1007		*NuSTAR*	60667007002	2021-05-08	30.7
		Chandra	7806	2007-03-20	14.8
F10038−3338		*NuSTAR*	60101055002	2016-01-14	53.3
		Chandra	7807	2007-03-07	14.4
F10565+2448	IRAS 10565+2448	*NuSTAR*	60001090002	2013-05-22	25.3
		Chandra	3952	2003-10-23	28.9
		XMM–Newton	0150320201	2003-06-17	22.4
F12112+0305		*NuSTAR*	60374005002	2018-01-17	15.3
		Chandra	4110	2003-04-15	10.0
		XMM–Newton	0081340801	2001-12-30	16.2
F12243−0036	NGC 4418	*NuSTAR*	60101052002	2015-07-03	43.8
		Chandra	4060	2003-03-10	19.8
F13126+2453	IC 860	*NuSTAR*	60301024002	2018-02-01	72.2
		Chandra	10400	2009-03-24	19.2
F14348−1447	F14348−1447 (NE and SW)	*NuSTAR*	60374004002	2018-01-27	21.0
		Chandra	6861	2006-03-12	14.7
		XMM–Newton	0081341401	2002-07-29	13.5
F14378−3651	IRAS 14378−3651	*NuSTAR*	60001092002	2013-02-28	24.4
		Chandra	7889	2007-06-25	13.9
F15250+3608		*NuSTAR*	60374009002	2018-01-17	16.8
		Chandra	4112	2003-08-27	9.8
		XMM–Newton	0081341101	2002-02-22	14.9
F17207−0014	IRAS F17207−0014	*NuSTAR*	60667001002	2020-08-01	20.6
		Chandra	2035	2001-10-24	48.5
		XMM–Newton	0081340601	2002-02-19	12.2

Table A1 – *continued*

(1) *IRAS* name	(2) Source	(3) Observatory	(4) Obs. ID	(5) Date	(6) Exposure (ks)
F18293−3413		*NuSTAR*	60101077002	2016-02-20	21.2
		Chandra	21379	2019-08-08	79.0
		XMM–Newton	0670300701	2012-03-16	16.0
F19297−0406		*NuSTAR*	60374007002	2018-03-03	20.0
		Chandra	7890	2007-06-18	16.4
F20550+1655	CGCG 448−020E and CGCG 448−020W	*NuSTAR*	60374002002	2018-03-28	24.9
		Chandra	7818	2007-09-10	14.6
		XMM–Newton	0670140101	2011-10-28	61.5
F20551−4250	ESO 286−IG19	*NuSTAR*	60101054002	2015-07-30	42.6
		Chandra	2036	2001-10-31	44.9
		XMM–Newton	0081340401	2001-04-21	10.1
F23128−5919	ESO 148−IG002	*NuSTAR*	60374006002	2018-03-07	27.0
		Chandra	2037	2001-09-30	49.3
		XMM–Newton	0081340301	2002-11-19	8.4
F23365+3604		*NuSTAR*	60667002002	2021-02-10	54.0
		Chandra	4115	2003-02-03	10.1

Table B1. The table reports the values obtained from the X-ray spectral analysis of the sources of our sample. For each source, we list (1) the *IRAS* name of the source, (2) the counterparts, (3) the column density of the X-ray emission associated with SF, (4) the temperature of the collisionally ionized plasma, (5) the photon index of the soft X-ray emission due to X-ray binaries or to the scattered emission from the AGN, (6) the column density and (7) the photon index of the AGN, and (8) the value of the Cash or χ^2 statistics and the number of degrees of freedom (DOF). Objects in which both statistics were used to fit different spectra are reported as $[C/\chi^2]$, and the value of the statistic (Stat) is the combination of the two.

(1) *IRAS* name	(2) Source	(3) $N_{\rm H}^{\rm SF}$ (10^{21} cm^{-2})	(4) kT (keV)	(5) $\Gamma_{\rm bin.}$	(6) $N_{\rm H}$ (10^{22} cm^{-2})	(7) Γ	(8) Stat/DOF
F00344−3349	ESO 350−IG038	$0.9^{+0.4}_{-0.3}$	$0.79^{+0.08}_{-0.09}$	$1.87^{+0.18}_{-0.17}$	–	–	294/330
F01053−1746	IC 1623A and IC 1623B	$0.8^{+0.2}_{-0.1}$	$0.73^{+0.03}_{-0.04}$	2.04 ± 0.08	–	–	1936/1931
F04454−4838	ESO 203−IG001	–	–	–	–	–	–
07251−0248		–	–	$4.4^{+2.8}_{-1.8}$	–	–	9.1/12
F08354+2555	NGC 2623	≤1.4	$1.1^{+0.5}_{-0.4}$	1.8[a]	$7.1^{+5.0}_{-2.8}$	1.8[b]	571/569
F08520−6850	ESO 060−IG16 (NE)	$8.3^{+6.5}_{-7.0}$	$0.12^{+1.09}_{-0.05}$	1.8[a]	15^{+10}_{-6}	1.8[b]	457/512
F08572+3915		–	–	0.7 ± 0.3	–	–	412/425
F09111−1007	W	–	–	1.4 ± 0.6	–	–	32/25
F09111−1007	E	–	–	2.2 ± 0.3	–	–	66/71
F10038−3338		7^{+8}_{-3}	$0.17^{+0.16}_{-0.10}$	$1.55^{+1.14}_{-0.85}$	–	–	74/71
10565+2448		$1.6^{+0.7}_{-0.6}$	$0.78^{+0.10}_{-0.12}$	$1.98^{+0.30}_{-0.26}$	–	–	536/617
F12112+0305		≤0.9	$0.93^{+0.13}_{-0.11}$	$1.45^{+0.45}_{-0.33}$	–	–	213/216
F12243−0036	NGC 4418	≤2.7	–	$1.65^{+0.81}_{-0.54}$	–	–	55/67
F13126+2453	IC 860	–	–	1.8[b]	–	–	22/17
F14348−1447	NE and SW	≤1.5	$0.94^{+0.36}_{-0.32}$	$1.42^{+0.41}_{-0.29}$	–	–	375/401
F14348−1447	NE	–	–	1.8 ± 0.7	–	–	26/21
F14348−1447	SW	–	–	1.2 ± 0.5	–	–	32/27
14378−3651		≤48	–	$2.7^{+3.4}_{-1.7}$	–	–	36/59
F15250+3608		≤1.2	$0.66^{+0.13}_{-0.37}$	$2.5^{+1.2}_{-0.6}$	–	–	220/230
F17207−0014		$8.0^{+1.7}_{-1.9}$	$0.29^{+0.12}_{-0.07}$	$1.60^{+0.31}_{-0.32}$	–	–	451/518
F18293−3413		$6.2^{+0.9}_{-1.2}$	$0.73^{+0.06}_{-0.08}$	$2.0^{+0.19}_{-0.21}$	–	–	1481/1570
F19297−0406		≤3.9	–	$2.5^{+0.9}_{-0.6}$	–	–	71/60
F20550+1655	CGCG 448−020E and CGCG 448−020W	$0.4^{+0.3}_{-0.2}$	$0.78^{+0.05}_{-0.06}$	$1.64^{+0.11}_{-0.10}$	–	–	1058/1092
	CGCG 448−020W	≤5.5	$0.82^{+0.21}_{-0.22}$	–	–	–	68/74
	CGCG 448−020E	$0.28^{+0.81}_{-0.27}$	$0.7^{+1.6}_{-0.3}$	$2.2^{+0.6}_{-0.8}$	–	–	62/85
F20551−4250	ESO 286−IG19	≤0.7	$0.82^{+0.05}_{-0.08}$	$1.60^{+0.29}_{-0.24}$	–	–	716/725
F23128−5919	ESO 148−IG002	≤0.1	$0.74^{+0.06}_{-0.08}$	$0.94^{+0.12}_{-0.13}$	–	–	741/798
F23365+3604		≤3.7	–	$1.33^{+0.96}_{-0.61}$	–	–	14/26

[a]Value of $\Gamma_{\rm bin.}$ fixed to that of the AGN continuum (Γ).
[b]Photon index fixed.

APPENDIX B: RESULTS OF THE X-RAY SPECTRAL ANALYSIS

The results of the spectral fitting performed here are reported in Table B1. Details on the spectral fitting approach can be found in Section 4.1.

APPENDIX C: INDIVIDUAL SOURCES

In the following, we report details on the X-ray spectral fitting of all new observations analysed here.

IRAS F00344−3349 (ESO 350−IG038): This late-stage merging galaxy is not detected by *NuSTAR*. The *Chandra* image shows an extended source, comprising three knots of SF, overlying both galaxies (Torres-Albà et al. 2018). The X-ray emission from this object is soft, with no clear hard X-ray component, and the SF model can reproduce very well the overall X-ray spectrum. Since this is a very close merger ($d_{\rm sep} = 1.1$ kpc), we follow the strategy of Torres-Albà et al. (2018), and consider the X-ray emission for the whole system.

IRAS F01053−1746 (IC 1623A and IC 1623B): The *Chandra* image of this advanced merger system shows an extended source in the 0.3–10 keV band, which covers both galaxies. As reported by Garofali et al. (2020), the 0.3–30 keV X-ray emission can be described by the superposition of several point sources and some diffuse emission, all ascribed to SF. The source is clearly detected by *NuSTAR*. In order to be consistent with the *XMM–Newton* and *NuSTAR* observations, we use an extraction radius of 20 arcsec for the *Chandra* observation, to encompass both sources. The overall X-ray spectrum is soft, and can be well reproduced by our SF model, consistent with Garofali et al. (2020).

IRAS F04454−4838 (ESO 203−IG001): Neither of the two galaxies in this early merger are detected by *Chandra* or *NuSTAR*. ESO 203−IG001 is the only object not detected by *Chandra* in Iwasawa et al. (2011).

IRAS 07251−0248: *Chandra* shows a faint point source consistent with this advanced merger. The X-ray spectrum could be well fitted by a simple power-law model.

IRAS F08354+2555 (NGC 2623): A hard point source is detected by *Chandra* coincident with the position of the advanced merger NGC 2623 (see also Torres-Albà et al. 2018). The source is also detected by both *XMM–Newton* and *NuSTAR*. As discussed in Ricci et al. (in preparation), this system shows clear [Ne V] emission from *Spitzer*/IRS spectra (Inami et al. 2013), which suggests that it hosts an AGN. Based on the *Chandra* hardness ratio, the source is also classified as a candidate obscured AGN by Torres-Albà et al. (2018). We therefore use our AGN model for the spectral fit, which was able to reproduce well the broad-band X-ray emission. We find that the AGN is only mildly obscured, and has one of the lowest column densities in our sample for an AGN in late-stage mergers ($N_{\rm H} = 7.1^{+10.7}_{-3.1} \times 10^{22}{\rm cm}^{-2}$).

IRAS F08520−6850 (ESO 060−IG16 NE and SW): This advanced merger (stage *c*) is detected both by *NuSTAR* and *Chandra*. A compact point source is detected in the *Chandra* image, overlapping with the nucleus of the NE galaxy (Iwasawa et al. 2011). The source shows [Ne V] emission in the MIR (Inami et al. 2013), and is classified as an AGN also considering the *Chandra* hardness ratio (Iwasawa et al. 2011). The X-ray spectrum is well fitted by the AGN model, with the X-ray source being obscured by a line-of-sight column density of $N_{\rm H} = 1.5^{+1.0}_{-0.6} \times 10^{23}\,{\rm cm}^{-2}$, consistent with what was previously found by Iwasawa et al. (2011) using the *Chandra* data.

IRAS F08572+3915: Only a faint detection of this double system is obtained by *Chandra* and *XMM–Newton*. *Chandra* shows a point-like hard X-ray component from the north-west nucleus (Iwasawa et al. 2011). The source is not detected by *NuSTAR*, from which we could infer an upper limit on the 10–24 keV luminosity of $\log(L_{10-24}/{\rm erg\,s}^{-1}) \leq 41.13$. The combined *XMM–Newton*/*Chandra* spectra could be well fitted by a simple power-law model, which returned a very low photon index ($\Gamma = 0.7 \pm 0.3$). Extending this model to higher energies would result in a 10–24 keV luminosity of $\log(L_{10-24}/{\rm erg\,s}^{-1}) = 41.46$, i.e. higher than the upper limit inferred from our *NuSTAR* observations, which suggests that this hard X-ray component is not associated with an obscured AGN.

IRAS F09111−1007: A point source was detected consistent with each of the two galaxies of this early merger. In both cases, the X-ray emission is rather faint, and it could be well fitted by a simple power-law model.

IRAS F10038−3338: A compact source is detected in the *Chandra* image, coincident with the position of this late-stage merger galaxy (Iwasawa et al. 2011). The source is not detected in the *NuSTAR* observation, and the X-ray spectrum is well fitted by the SF model.

IRAS 10565+2448: *Chandra* detects a point source coincident with the western member of this advanced merger (Iwasawa et al. 2011). The source is not detected by *NuSTAR*, and the X-ray spectrum is accurately modelled using the SF model.

IRAS F12112+0305: The *Chandra* image shows two sources, coincident with the two optical nuclei (Iwasawa et al. 2011). The combined *Chandra*/*XMM–Newton* spectrum is well fitted by our SF model. The source is not detected by *NuSTAR*.

IRAS F12243−0036 (NGC 4418): Two point sources are found at a distance of ∼1.5 arcsec from each other in the *Chandra* images, with the eastern source being brighter above ∼2 keV (Torres-Albà et al. 2018). The source is not detected by *NuSTAR*, and the X-ray spectrum is well fitted with our SF model.

IRAS F13126+2453 (IC 860): The source is only faintly detected by *Chandra*, and is not detected by *NuSTAR*. Due to the low signal-to-noise ratio of the spectrum, we fit it using a simple power-law model, with the photon index fixed to $\Gamma = 1.8$.

IRAS F14348−1447 (NE and SW): The *Chandra* image shows some diffuse X-ray emission, together with two point sources, with the southern one being brighter (Iwasawa et al. 2011). The source is not detected by *NuSTAR*, and our SF model can well represent the X-ray spectrum. We also looked at the individual properties of the two nuclei in the *Chandra* observations, selecting circular regions of 2 arcsec around the sources. Due to the low signal-to-noise ratio, the two spectra are fitted with a simple power-law model.

IRAS 14378−3651: *Chandra* shows the presence of a point-like source consistent with the nucleus of the galaxy, plus some soft, extended, X-ray emission (Iwasawa et al. 2011). The source is not detected by *NuSTAR*, and the X-ray emission is well represented by a power-law component.

IRAS F15250+3608: The source is detected by both *Chandra* and *XMM–Newton*, with the former showing a soft point source with a position consistent with that of the optical counterpart (Iwasawa et al. 2011). IRAS F15250+3608 is not detected by *NuSTAR*, and its X-ray spectrum is well fitted by the SF model.

IRAS F17207−0014: This *d*-stage, single-nucleus merger is detected by *Chandra*, exhibiting two peaks, with the southern one being harder and coinciding with the position of the optical nucleus of the system (Iwasawa et al. 2011). The source is also detected by *XMM–Newton*, but it is not detected by *NuSTAR*. The SF model provides a good fit to the X-ray spectrum.

IRAS F18293−3413: *Chandra* shows resolved X-ray emission in both the soft and hard bands (Iwasawa et al. 2011) of this minor merger, classified as stage *N* (Ricci et al. 2017b). The source is

detected by both *XMM–Newton* and *NuSTAR*, albeit for the latter only in the 3–10 keV band. The combined spectra can be well represented by the SF model plus an additional emission feature, associated with Fe XXV (e.g. Iwasawa et al. 2009). The data show in fact an excess at ∼6.6 keV, which can be well represented by a Gaussian line with a width fixed to $\sigma = 10$ eV, and energy of $6.64^{+0.12}_{-0.11}$ keV. The equivalent width of the line is 360^{+181}_{-162} eV. A detailed analysis of Fe K α emission lines in GOALS objects will be presented in a forthcoming dedicated paper (Iwasawa et al., in preparation).

IRAS F19297−0406: The soft X-ray emission detected by *Chandra* for this late merger with a single nucleus is extended, while the hard X-ray emission is compact (Iwasawa et al. 2011). This object is not detected by *NuSTAR*, and we use a simple power-law model to reproduce its X-ray emission.

IRAS F20550+1655 (CGCG 448−020E and CGCG 448−020W): This late merger, with two nuclei separated by 5 arcsec, is detected by both *Chandra* and *XMM–Newton*, but is not detected by *NuSTAR*. *Chandra* shows some diffuse X-ray emission, with two rather compact hard X-ray sources (Iwasawa et al. 2011). The X-ray spectrum is well fitted by the SF model.

IRAS F20551−4250 (ESO 286−IG19): This system is a late-stage merger with a single nucleus, which is clearly detected by *Chandra* and *XMM–Newton*, but it is not detected by *NuSTAR*. The soft X-ray emission observed in *Chandra* is elongated, consistent with an SF-related origin, while the hard X-ray emission is point-like, with some fainter elongation (Iwasawa et al. 2011). Our fit with the SF model leaves clear residuals around ∼6 keV. We tested our AGN model, fixing $\Gamma = 1.8$ (e.g. Ricci et al. 2017c), and found that it provides a significant improvement on the fit. However, the expected 10–24 keV luminosity from this model ($L_{10-24} = 1.3 \times 10^{42}$ erg s^{-1}) is above the upper limit obtained by our *NuSTAR* observations ($L_{10-24} \leq 3.2 \times 10^{41}$ erg s^{-1}). This suggests that the excess is not associated with an AGN. Including a Gaussian line to the SF model, with width fixed to 10 eV, improved the fit; the energy of the line is $6.60^{+0.05}_{-0.06}$ keV, which suggests emission from Fe XXV.

IRAS F23128−5919 (ESO 148−IG002): This system is a late-stage merger, which is well detected by *Chandra* and *XMM–Newton*, and is not detected by *NuSTAR*. The *Chandra* image shows extended X-ray emission, which covers both galactic nuclei. The X-ray spectrum is well fitted by our SF model. Franceschini et al. (2003) report the presence of an AGN absorbed by a column density of $N_{\rm H} \sim 7 \times 10^{22}$ cm^{-2}, and Iwasawa et al. (2011) discuss that the AGN might be associated with the southern nucleus. We apply our AGN model, fixing $\Gamma = 1.8$ (e.g. Ricci et al. 2017c), finding a very similar column density ($N_{\rm H} = 7^{+5}_{-2} \times 10^{22}$ cm^{-2}). However, the expected observed 10–24 keV luminosity from this model (8.3×10^{41} erg s^{-1}) is higher than the upper limit inferred by our *NuSTAR* observations ($L_{10-24} \leq 1.7 \times 10^{41}$ erg s^{-1}). This implies that, if an AGN is present in this system, it is significantly more obscured than what is reported by Franceschini et al. (2003), and the observed X-ray emission of this object is thus dominated by SF. We therefore used the SF model for this object.

IRAS F23365+3604: *Chandra* shows a point-like source coinciding with the nucleus of this late merger. The source is not detected by *NuSTAR*, and its X-ray spectrum is well fitted by a simple power-law model.

[1]*Núcleo de Astronomía de la Facultad de Ingeniería, Universidad Diego Portales, Av. Ejército Libertador 441, Santiago 22, Chile*
[2]*Kavli Institute for Astronomy and Astrophysics, Peking University, Beijing 100871, China*
[3]*National Radio Astronomy Observatory, 520 Edgemont Road, Charlottesville, VA 22903, USA*
[4]*Department of Physics & Astronomy, George Mason University, MS 3F3, 4400 University Drive, Fairfax, VA 22030, USA*
[5]*IPAC, California Institute of Technology, 1200 E. California Boulevard, Pasadena, CA 91125, USA*
[6]*Institut de Ciències del Cosmos, Universitat de Barcelona, IEEC-UB, Martí i Franquès, 1, E-08028 Barcelona, Spain*
[7]*ICREA, Pg. Lluís Companys, 23, E-08010 Barcelona, Spain*
[8]*Kinard Laboratory of Physics, Clemson University, Clemson, SC 29634, USA*
[9]*Instituto de Astrofísica and Centro de Astroingeniería, Facultad de Física, Pontificia Universidad Católica de Chile, Casilla 306, Santiago 22, 8970117, Chile*
[10]*Millennium Institute of Astrophysics, Nuncio Monseor Stero Sanz 100, Providencia, Santiago 8010000, Chile*
[11]*Space Science Institute, 4750 Walnut Street, Suite 205, Boulder, CO 80301, USA*
[12]*Department of Astronomy, School of Physics, Peking University, Beijing 100871, China*
[13]*Department of Space, Earth and Environment, Chalmers University of Technology, Onsala Space Observatory, SE-439 92 Onsala, Sweden*
[14]*Instituto de Física y Astronomía, Facultad de Ciencias, Universidad de Valparaíso, Gran Bretana N1111, Playa Ancha, Valparaíso, 2340000, Chile*
[15]*Department of Physics, University of Crete, Heraklion GR-71003, Greece*
[16]*Institute of Astrophysics, Foundation for Research and Technology – Hellas, Heraklion GR-70013, Greece*
[17]*Department of Astronomy, University of Virginia, Charlottesville, VA 22904, USA*
[18]*Department of Astronomy, Beijing Normal University, Beijing 100875, China*
[19]*Hiroshima Astrophysical Science Center, Hiroshima University, 1-3-1 Kagamiyama, Higashi-Hiroshima, Hiroshima 739-8526, Japan*
[20]*Eureka Scientific, 2452 Delmer Street Suite 100, Oakland, CA 94602-3017, USA*
[21]*European Southern Observatory, Karl-Schwarzschild-Strasse 2, D-85748 Garching, Germany*
[22]*Department of Astronomy, University of Massachusetts at Amherst, Amherst, MA 01003, USA*
[23]*Ritter Astrophysical Research Center, University of Toledo, Toledo, OH 43606, USA*
[24]*ARC Centre of Excellence for All Sky Astrophysics in 3 Dimensions (ASTRO 3D)*
[25]*Institute for Astronomy, University of Hawaii, 2680 Woodlawn Drive, Honolulu, HI 96822, USA*
[26]*Jet Propulsion Laboratory, California Institute of Technology, 4800 Oak Grove Drive, MS 169-224, Pasadena, CA 91109, USA*
[27]*Department of Physics and Astronomy, University of California, 4129 Frederick Reines Hall, Irvine, CA 92697, USA*
[28]*Department of Astronomy, Kyoto University, Kitashirakawa-Oiwake-cho, Sakyo-ku, Kyoto 606-8502, Japan*

This paper has been typeset from a TEX/LATEX file prepared by the author.